Astronomy & Astrophysics manuscript no. Planck2014_systematics
February 10, 2016

Planck 2015 results. III. LFI systematic uncertainties

Planck Collaboration: P. A. R. Ade[77], J. Aumont[53], C. Baccigalupi[75], A. J. Banday[82,8], R. B. Barreiro[58], N. Bartolo[27,59], S. Basak[75], P. Battaglia[29,31], E. Battaner[83,84], K. Benabed[54,81], A. Benoit-Lévy[21,54,81], J.-P. Bernard[82,8], M. Bersanelli[30,45], P. Bielewicz[73,8,75], A. Bonaldi[61], L. Bonavera[58], J. R. Bond[7], J. Borrill[11,78], C. Burigana[44,28,46], R. C. Butler[44], E. Calabrese[80], A. Catalano[68,66], P. R. Christensen[74,33], L. P. L. Colombo[20,60], M. Cruz[17], A. Curto[58,5,63], F. Cuttaia[44], L. Danese[75], R. D. Davies[61], R. J. Davis[61], P. de Bernardis[29], A. de Rosa[44], G. de Zotti[41,75], J. Delabrouille[1], C. Dickinson[61], J. M. Diego[58], O. Doré[60,9], A. Ducout[54,51], X. Dupac[34], F. Elsner[21,54,81], T. A. Enßlin[71], H. K. Eriksen[56], F. Finelli[44,46], M. Frailis[43], C. Franceschet[30], E. Franceschi[44], S. Galeotta[43], S. Galli[62], K. Ganga[1], T. Ghosh[53], M. Giard[82,8], Y. Giraud-Héraud[1], E. Gjerløw[56], J. González-Nuevo[16,58], K. M. Górski[60,85], A. Gregorio[31,43,49], A. Gruppuso[44], F. K. Hansen[56], D. L. Harrison[55,63], C. Hernández-Monteagudo[10,71], D. Herranz[58], S. R. Hildebrandt[60,9], E. Hivon[54,81], M. Hobson[5], A. Hornstrup[13], W. Hovest[71], K. M. Huffenberger[22], G. Hurier[53], A. H. Jaffe[51], T. R. Jaffe[82,8], E. Keihänen[23], R. Keskitalo[11], K. Kiiveri[23,39], T. S. Kisner[70], J. Knoche[71], N. Krachmalnicoff[30], M. Kunz[14,53,2], H. Kurki-Suonio[23,39], G. Lagache[4,53], J.-M. Lamarre[66], A. Lasenby[5,63], M. Lattanzi[28], C. R. Lawrence[60], J. P. Leahy[61], R. Leonardi[6], F. Levrier[66], M. Liguori[27,59], P. B. Lilje[56], M. Linden-Vørnle[13], V. Lindholm[23,39], M. López-Caniego[34,58], P. M. Lubin[25], J. F. Macías-Pérez[68], B. Maffei[61], G. Maggio[43], D. Maino[30,45], N. Mandolesi[44,28], A. Mangilli[53,65], M. Maris[43], P. G. Martin[7], E. Martínez-González[58], S. Masi[29], S. Matarrese[27,59,36], P. R. Meinhold[25], A. Mennella[30,45], M. Migliaccio[55,63], S. Mitra[50,60], L. Montier[82,8], G. Morgante[44], D. Mortlock[51], D. Munshi[77], J. A. Murphy[72], F. Nati[24], P. Natoli[28,3,44], F. Noviello[61], F. Paci[75], L. Pagano[29,47], F. Pajot[53], D. Paoletti[44,46], B. Partridge[38], F. Pasian[43], T. J. Pearson[9,52], O. Perdereau[65], V. Pettorino[37], F. Piacentini[29], E. Pointecouteau[82,8], G. Polenta[3,42], G. W. Pratt[67], J.-L. Puget[53], J. P. Rachen[18,71], M. Reinecke[71], M. Remazeilles[61,53,1], A. Renzi[32,48], I. Ristorcelli[82,8], G. Rocha[60,9], C. Rosset[1], M. Rossetti[30,45], G. Roudier[1,66,60], J. A. Rubiño-Martín[57,15], B. Rusholme[52], M. Sandri[44], D. Santos[68], M. Savelainen[23,39], D. Scott[19], V. Stolyarov[5,79,64], R. Stompor[1], A.-S. Suur-Uski[23,39], J.-F. Sygnet[54], J. A. Tauber[35], D. Tavagnacco[43,31], L. Terenzi[76,44], L. Toffolatti[16,58,44], M. Tomasi[30,45], M. Tristram[65], M. Tucci[14], G. Umana[40], L. Valenziano[44], J. Valiviita[23,39], B. Van Tent[69], T. Vassallo[43], P. Vielva[58], F. Villa[44], L. A. Wade[60], B. D. Wandelt[54,81,26], R. Watson[61], I. K. Wehus[60,56], D. Yvon[12], A. Zacchei[43], J. P. Zibin[19], and A. Zonca[25]

(Affiliations can be found after the references)

February 10, 2016

ABSTRACT

We present the current accounting of systematic effect uncertainties for the Low Frequency Instrument (LFI) that are relevant to the 2015 release of the *Planck* cosmological results, showing the robustness and consistency of our data set, especially for polarization analysis. We use two complementary approaches: (i) simulations based on measured data and physical models of the known systematic effects; and (ii) analysis of difference maps containing the same sky signal ("null-maps"). The LFI temperature data are limited by instrumental noise. At large angular scales the systematic effects are below the cosmic microwave background (CMB) temperature power spectrum by several orders of magnitude. In polarization the systematic uncertainties are dominated by calibration uncertainties and compete with the CMB E-modes in the multipole range 10–20. Based on our model of all known systematic effects, we show that these effects introduce a slight bias of around $0.2\,\sigma$ on the reionization optical depth derived from the 70 GHz EE spectrum using the 30 and 353 GHz channels as foreground templates. At 30 GHz the systematic effects are smaller than the Galactic foreground at all scales in temperature and polarization, which allows us to consider this channel as a reliable template of synchrotron emission. We assess the residual uncertainties due to LFI effects on CMB maps and power spectra after component separation and show that these effects are smaller than the CMB amplitude at all scales. We also assess the impact on non-Gaussianity studies and find it to be negligible. Some residuals still appear in null maps from particular sky survey pairs, particularly at 30 GHz, suggesting possible straylight contamination due to an imperfect knowledge of the beam far sidelobes.

Key words. Cosmology: cosmic background radiation – observations – Space vehicles: instruments – Methods: data analysis

1. Introduction

This paper, one of a set associated with the 2015 release of data from the *Planck*[1] mission, describes the Low Frequency Instrument (LFI) systematic effects and their related uncertainties in cosmic microwave background (CMB) temperature and polarization scientific products. Systematic effects in the High Frequency Instrument data are discussed in Planck Collaboration VII (2016) and Planck Collaboration VIII (2016).

The 2013 *Planck* cosmological data release (Planck Collaboration I 2014) exploited data acquired during the first 14 months of the mission to produce the most accurate (to date) all-sky CMB temperature map and power spectrum in terms of sensitivity, angular resolution, and rejection of astrophysical and instrumental systematic effects. In Planck Collaboration III (2014) we showed that known and unknown systematic uncertainties are at least two orders of magnitude below the CMB temperature power spectrum, with residuals dominated by Galactic straylight and relative calibration uncertainty.

The 2015 release (Planck Collaboration I 2016) is based on the entire mission (48 months for LFI and 29 months for HFI). For LFI, the sensitivity increase compared to the 2013 release is a approximately a factor of two on maps. This requires a thor-

[1] *Planck* (http://www.esa.int/Planck) is a project of the European Space Agency (ESA) with instruments provided by two scientific consortia funded by ESA member states and led by Principal Investigators from France and Italy, telescope reflectors provided through a collaboration between ESA and a scientific consortium led and funded by Denmark, and additional contributions from NASA (USA).

ough assessment of the level of systematic effects to demonstrate the robustness of the results and verify that the final uncertainties are noise-limited.

We evaluate systematic uncertainties via two complementary approaches: (i) using null maps[2] to highlight potential residual signatures exceeding the white noise. We call this a "top-down" approach; (ii) simulating all the known systematic effects from time-ordered data to maps and power spectra. We call this a "bottom-up" approach. This second strategy is particularly powerful, because it allows us to evaluate effects that are below the white noise level and do not show up in our null maps. Furthermore, it allows us to assess the impact of residual effects on Gaussianity studies and component separation.

In this paper we provide a comprehensive study of the instrumental systematic effects and the uncertainties that they cause on CMB maps and power spectra, in both temperature and polarization.

We give the details of the analyses leading to our results in Sects. 2 and 3 . In Sect. 2 we discuss the instrumental effects that were not treated in the previous release. Some of these effects are removed in the data processing pipeline according to algorithms described in Planck Collaboration II (2016). In Sect. 3 we assess the residual systematic effect uncertainties according to two complementary "top-down" and "bottom-up" approaches.

We present the main results in Sect. 4, which provides an overview of all the main findings. We refer, in particular, to Tables 5, 6 and 7 for residual uncertainties on maps and Figs. 24 through 27 for the impact on power spectra. These figures contain the power spectra of the systematic effects and are often referred to in the text, so we advise the reader to keep them at hand while going through the details in Sects. 2 and 3.

This paper requires a general knowledge of the design of the LFI radiometers. For a detailed description we recommend reading section 3 of Bersanelli et al. (2010). Otherwise the reader can find a brief and simple description in section 2 of Mennella et al. (2011). Throughout this paper we follow the naming convention described in appendix A of Mennella et al. (2010) and also available on-line in the Explanatory Supplement.[3]

2. LFI systematic effects affecting LFI data

In this section we describe the known systematic effects affecting the LFI data, and list them in Table 1.

Several of these effects were already discussed in the context of the 2013 release (Planck Collaboration III 2014), so we do not repeat the full description here. They are:

- white noise correlation;
- $1/f$ noise;
- bias fluctuations;
- thermal fluctuations (20-K front-end unit, 300-K back-end unit, 4-K reference loads);
- so-called "1-Hz" spikes, caused by the housekeeping acquisition clock;
- analog-to-digital converter nonlinearity.

Here we describe effects that are either polarization-specific or that have been treated differently in this data release. These effects are:

- near sidelobes pickup;
- far sidelobes pickup;
- imperfect photometric calibration;
- pointing uncertainties;
- bandpass mismatch;
- polarization angle uncertainties.

Two other effects that are listed in Table 1 but are not discussed in this paper are: (i) main beam ellipticity, and (ii) orthomode transducer cross-polarization. The first is discussed in sections 5 and 6 of Planck Collaboration IV (2016). The second is negligible for LFI, as it is shown in section 4.1 of Leahy et al. (2010).

2.1. Optics and pointing

2.1.1. Far sidelobes

The far sidelobes are a source of systematic error because they pick up radiation far from the telescope line of sight and give rise to so-called "straylight contamination." The LFI 30 GHz channel is particularly sensitive to the straylight contamination, because the diffuse Galactic emission components are rather strong at this frequency, and the far-sidelobe level of the 30 GHz beams is significantly higher compared to the other frequencies (for more details, see Sandri et al. 2010). The simulated pattern shown in Fig. 1 provides an example of the far sidelobes of a 70 GHz radiometer. The plot is a cut passing through the main reflector spillover of the *Planck* telescope [4].

Straylight impacts the measurements in two ways: it directly contaminates the maps; and it affects the photometric calibration. In the latter case, the straylight could be a significant fraction of the measured signal that is compared with the calibrator itself (i.e., the Dipole), causing a systematic error in the recovered calibration constants. This error varies with time, depending on the orientation of the Galactic plane with respect to the line of sight.

In the 2013 release we did not correct the LFI data for the straylight contamination and simply estimated the residual uncertainty in the final maps and power spectra (see table 2 and figure 1 of Planck Collaboration III 2014).

In the CMB polarization analysis, instead, we accounted for this effect, both in the calibration phase and in the production of the calibrated timelines. This is particularly relevant at 30 GHz, while at 44 and 70 GHz the straylight spurious signal is small compared to the CMB, both in temperature and polarization (see the green dotted spectra in Figs. 24, 25 and 26).

We perform straylight correction in two steps: first, we calibrate the data, accounting for the straylight contamination in the sky signal; and then we remove it from the data themselves. To estimate the straylight signal, we assume a fiducial model of the sidelobes based on GRASP beams and radiometer band shapes, as well as a fiducial model of the sky emission based on simulated temperature and polarization maps. We discuss the details of these procedures in sections 7.1 and 7.4 of Planck Collaboration II (2016) and section 2 of Planck Collaboration V (2016).

2.1.2. Near sidelobes

The "near sidelobes" are defined as the lobes in the region of the beam pattern in the angular range extending between the main beam angular limit[5] and 5°(see Fig. 1) . We see that the power

[2] A null map is the difference between maps over time periods in which the sky signal is the same. See Sect. 3.3

[3] http://wiki.cosmos.esa.int/planckpla/index.php/Main_Page

[4] For the definition of the main- and sub-reflector spillovers refer to figure 7 of Planck Collaboration III (2014)

[5] The main beam is defined as extending to 1.9, 1.3, and 0.9° at 30, 44, and 70 GHz, respectively.

Table 1: List of known instrumental systematic effects in *Planck*-LFI.

Effect	Source	Control/Removal	Reference
Effects independent of the sky signal (temperature and polarization)			
White noise correlation	Phase switch imbalance	Diode weighting	Planck Collaboration III (2014)
$1/f$ noise	RF amplifiers	Pseudo-correlation and destriping	Planck Collaboration III (2014)
Bias fluctuations	RF amplifiers, back-end electronics	Pseudo-correlation and destriping	3.2.5
Thermal fluctuations	4-K, 20-K and 300-K thermal stages	Calibration, destriping	3.2.4
1-Hz spikes	Back-end electronics	Template fitting and removal	3.2.6
Effects dependent on the sky signal (temperature and polarization)			
Main beam ellipticity	Main beams	Accounted for in window function	Planck Collaboration III (2016)
Near sidelobe pickup	Optical response at angles $< 5°$ from the main beam	Masking of Galaxy and point sources	Planck Collaboration II (2016), 2.1.2, 3.2.1
Far sidelobe pickup	Main and sub-reflector spillover	Model sidelobes removed from timelines	2.1.1, 3.2.1
Analogue-to-digital converter nonlinearity	Back-end analogue-to-digital converter	Template fitting and removal	3.2.3
Imperfect photometric calibration	Sidelobe pickup, radiometer noise temperature changes, and other non-idealities	Adaptive smoothing algorithm using 4π beam, 4-K reference load voltage output, temperature sensor data	Planck Collaboration II (2016), 2.2, 3.2.2
Pointing	Uncertainties in pointing reconstruction, thermal changes affecting focal plane geometry	Negligible impact on anisotropy measurements	2.1, 3.2.1
Effects specifically impacting polarization			
Bandpass asymmetries	Differential orthomode transducer and receiver bandpass response	Spurious polarization removal	2.3
Polarization angle uncertainty	Uncertainty in the polarization angle in-flight measurement	Negligible impact	2.1.3, 3.2.1
Orthomode transducer cross-polarization	Imperfect polarization separation	Negligible impact	Leahy et al. (2010)

level of near sidelobes is about −40 dB at 30 GHz, and −50 dB at 70 GHz, with the shape of a typical diffraction pattern.

Near sidelobes can be a source of systematic effects when the main beam scans the sky near the Galactic plane or in the proximity of bright sources. In the parts of the sky dominated by diffuse emission with little contrast in intensity, these lobes introduce a spurious signal of about 10^{-5} times the power entering the main beam.

We expect that the effect of near sidelobes on CMB measurements is small, provided that we properly mask the Galactic plane and the bright sources. For this reason we did not remove such an effect from the data and assessed its impact by generating simulated sky maps observed with and without the presence of near sidelobes in the beam and then taking the difference. We show and discuss such maps in Sect. 3.2.1 and the power spectra of this effect in Figs. 24, 25 and 26.

2.1.3. Polarization angle

We now discuss the systematic effect caused by the uncertainty in the orientation of the feed-horns in the focal plane. From thermo-elastic simulations we found this uncertainty to be about 0.2° (Villa et al. 2005). In this study we adopt a more conservative approach in which we set the uncertainties using measurements of the Crab Nebula. Then we perform a sensitivity study in which we consider a fiducial sky observed with a certain polarization angle for each feed-horn and then reconstruct the sky with a slightly different polarization angle for each feed horn. The differences span the range of uncertainties in the polarization angle derived from measurements of the Crab Nebula.

In this section we first recall our definition of polarization angle and then we discuss the rationale we used to define the "error bars" used in our sensitivity study.

Definition of polarization angle. Each LFI scanning beam[6] is defined in a reference frame specified by the three angles $\theta_{\rm uv}$, $\phi_{\rm uv}$, and $\psi_{\rm uv}$, reported in table 5 of Planck Collaboration II (2016) and shown in Fig. 2. This choice implies that the power peak of the co-polar component lies along the main beam pointing direction, and a minimum in the cross-polar component appears in the same direction (Planck Collaboration IV 2016). In particular, the major axis of the polarization ellipse is along the

[6] Here we refer to both the beams simulated with GRASP and to those reconstructed from Jupiter transits.

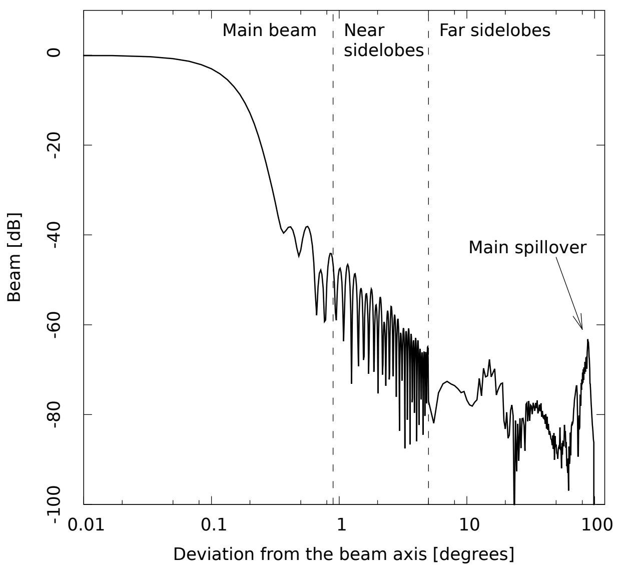

Fig. 1: Example of a cut of the simulated beam pattern of the 70 GHz `LFI18-S` radiometer. The cut passes through the main reflector spillover of the *Planck* telescope. The plot shows, in particular, the level and shape of the near sidelobes.

x-axis for the radiometer side arm (`S`) and it is aligned with the y-axis for the radiometer main arm (`M`).

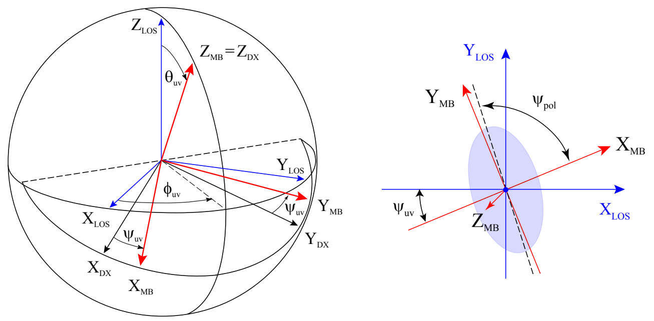

Fig. 2: Definition of polarization angle. *Left*: the orientation of the main beam frame, $(XYZ)_{MB}$, with respect to the line-of-sight (LOS) frame, $(XYZ)_{LOS}$, is defined by the three angles θ_{uv}, ϕ_{uv}, and ψ_{uv}. The intermediate frame, $(XYZ)_{DX}$, is the detector frame, defined by the two angles θ_{uv} and ϕ_{uv}. *Right*: the angle ψ_{pol} is defined with respect to X_{MB} and represents the orientation of the polarization ellipse along the beam line-of-sight. It is very close to 0 or 90 degrees for the `S` and `M` radiometers, respectively.

The main beam is essentially linearly polarized in directions close to the beam pointing. The x-axis of the main beam frame can be assumed to be the main beam polarization direction for the `S` radiometers and the y-axis of the main beam frame can be assumed to be the main beam polarization direction for the `M` radiometers.

We define ψ_{pol} to be the angle between the main beam polarization direction and the x-axis of the main beam frame, and define the main beam polarization angle, ψ, as $\psi = \psi_{uv} + \psi_{pol}$. The angle ψ_{pol} is nominally either 0° or 90° for the side and main arms, respectively.

The values of ψ_{pol} can be either determined from measured data using the Crab Nebula as a calibrator, or from optical simulations performed coupling the LFI feedhorns to the *Planck* telescope, considering both the optical and radiometer bandpass response.[7]

For the current release our analysis uses values of ψ_{pol} derived from simulations. Indeed, the optical model is well constrained by the main beam reconstruction carried out with seven Jupiter transits and provides us with more accurate estimates of the polarization angle compared to direct measurements.

As an independent crosscheck, we also consider our measurements of the Crab nebula as a polarized calibrating source. We use a least-squares fit of the time-ordered data measured during Crab scans to determine I, Q, and U and, consequently, the polarization angle. Then we incorporate the instrument noise via the covariance matrix and we obtain the final error bars by adding in quadrature the uncertainties due to the bandpass mismatch correction (Planck Collaboration II 2016).

While such a check is desirable, we find that the polarization angles derived from these data display systematic errors much larger than those expected from our noise and bandpass mismatch correction alone, especially at 30 and 44 GHz (horns from `LFI24` through `LFI28`) (see Fig. 3). In particular, we find that the values obtained for the various horns in the focal plane display differences that are larger than our error estimates.

The horn with the largest apparent offset in angle, `LFI25`, is the solitary 44 GHz horn on one side of the focal plane; in the next data release we will examine this discrepancy in more detail.

An important difficulty is the determination of the relative gains of the individually polarized receivers, particularly during the Crab crossings, which appear near the minima of our principal temperature calibration. Another souce of uncertainty missing from the Crab analysis is beam errors. Of course, the LFI radiometer polarization angles are not changing over time, but the variability in the estimates limits our use of the Crab crossings for this purpose.

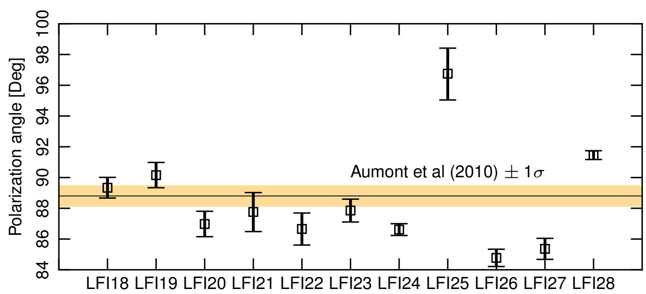

Fig. 3: Crab Nebula polarization angle measured by the various feed-horns in the focal plane. The straight horizontal line reports the value from Aumont et al. (2010) converted to Galactic coordinates, and the yellow area is the $\pm 1\,\sigma$ uncertainty.

Definition of error bars. The ψ_{pol} angle can differ from its nominal value because of small misalignments induced by

[7] The polarization angle is defined as $\psi_{pol} = \arctan(E_{rhc}/E_{lhc})$. Here E_{rhc} and E_{lhc} are the right- and left-hand circularly polarized components of the field, which can be defined in terms of the co- and cross-polar components, E_{co} and E_{cx}, as $E_{rhc(lhc)} = (E_{co} - (+)\, E_{cx})/\sqrt{2}$ (TICRA Engineering Consultants 2008).

the mechanical tolerances, thermo-mechanical effects during cooldown, and by uncertainties in the the optical and radiometer behavior across the band. If we consider the variation of $\psi_{\rm pol}$ across the band in our simulations, for example, we find deviations from the nominal values that are, at most, $0.5°$.

To estimate the impact of imperfect knowledge of the polarization angle on CMB maps, we use the errors derived in the Crab analysis, which include the scan strategy and white noise and bandpass mismatch correction errors. While the errors derived this way are not designed to capture the time variation of the actual Crab measurements, we believe they provide a conservative upper bound to the errors in our knowledge of the instrument polarization angles.

The two panels in Fig. 4 show the values of $\psi_{\rm pol}$ derived from `GRASP` simulations (which are also used by the data analysis pipeline) and the error bars obtained from Crab observations. Notice that the scatter of the simulated angles is much less than the size of the error bars. This is consistent with uncertainty on the simulated angles that is much smaller than the error bars derived from Crab measurements. These data are the basis of the simulation exercise discussed in Sect. 3.2.1.

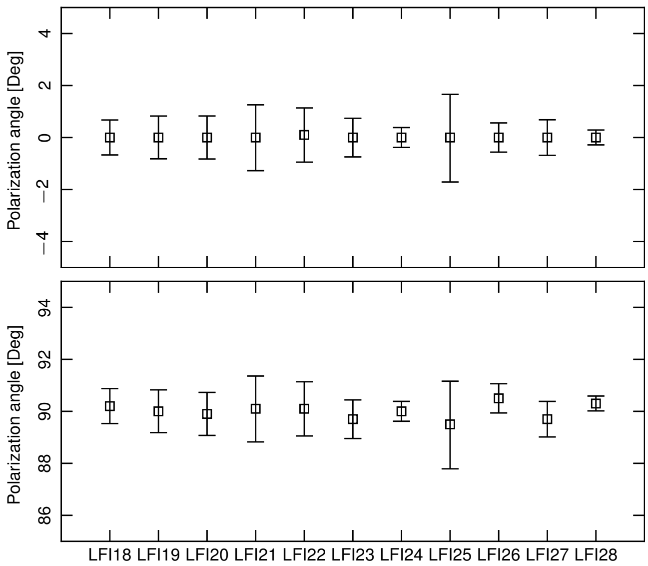

Fig. 4: Simulated polarization angles and error bars from Crab measurements used in the analysis. *Top*: radiometer main arm. *Bottom*: radiometer side arm. The scatter of the plotted angles is much less than the error bars because the uncertainty in our simulations is much smaller than the error bars derived from Crab measurements.

Our on-ground determination of radiometer polarization angles is more than sufficient for the CMB polarization. As seen in the measurements of the Crab Nebula, the impact of gain errors among our polarized radiometers may be important, and we do include this effect in our gain error simulations.

2.1.4. Pointing

Pointing reconstruction is performed in two steps. The first is the reconstruction of the satellite attitude, the second is the measurement of the orientation of the individual detectors with respect to the focal plane boresight (focal plane geometry reconstruction). In the first step we take into account all common-mode variations between the star camera and focal plane frames and assume the focal plane reconstruction, so that the focal plane geometry is essentially fixed over the entire mission.

Planet scans indicate that the satellite attitude, reconstructed from the star camera data, contains slow timescale variations ($\gtrsim$ 1 month) leading to total errors up to about $30''$. The two major modes are a linear drift and a modulation that is heavily correlated with the Sun-Earth distance. To correct these fluctuations we fit a linear drift and a solar distance template to the planet position offsets, and include discontinuous steps at known disturbances of the thermal environment. Further details about the pointing reconstruction can be found in section 5.3 of Planck Collaboration I (2016).

In this paper we evaluate the impact on the CMB maps and power spectra of residual uncertainties in the pointing reconstruction process. We perform the assessment using simulations in which the same sky is observed with two different pointing solutions that represent the uncertainty upper limit. We describe the approach and the results obtained in Sect. 3.2.1.

2.2. Imperfect calibration

The analysis of the first data release showed that the uncertainty in the calibration is one of the main factors driving the systematic effects budget for *Planck*-LFI. The accuracy of the retrieved calibration constant depends on the signal-to-noise ratio (S/N) between the dipole and instrumental noise along the scan directions, on effects causing gain variations (e.g., focal plane temperature fluctuations), and on the presence of Galactic straylight in the measured signal.

In the analysis for the 2015 release we have substantially revised our calibration pipeline to account for these effects and to improve the accuracy of the calibration. The full details are provided in Planck Collaboration V (2016), and here we briefly list the most important changes: (i) we derive the Solar dipole parameters using LFI-only data, so that we no longer rely on parameters provided by Hinshaw et al. (2009); (ii) we take into account the shape of the beams over the full 4π sphere; (iii) we use an improved iterative calibration algorithm to estimate the calibration constant K (measured in $\mathrm{V\,K^{-1}}$);[8] and (iv) we use a new smoothing algorithm to reduce the statistical uncertainty in the estimates of K and to account for gain changes caused by variations in the instrument environment.

We nevertheless expect residual systematic effects in the calibration constants due to uncertainties in the following pipeline steps.

1. Solar dipole parameters derived from LFI data. This affects only the absolute calibration and impacts the overall dynamic range of the maps, as well as the power spectrum level. We discuss the absolute calibration accuracy in Planck Collaboration V (2016) and do not address it further here.
2. Optical model and radiometer bandpass response. This enters the computation of the 4π beams, which are used to account for Galactic straylight in the calibration.
3. A number of effects (e.g., the impact of residual Galactic foregrounds) that might bias the estimates of the calibration constant K.
4. The smoothing filter we use to reduce the scatter in the values of K near periods of dipole minima might be too aggressive, removing features from the set of K measurements that are

[8] We have implemented such improvements into a new module named `DaCapo`, described in section 7.1 of Planck Collaboration II (2016).

not due to noise. This could cause systematic errors in the temperature and polarization data.

We estimate the residual calibration uncertainties using simulations, as discussed in Sect. 3.2.2. For this release we neglect effects caused by imperfect knowledge of the far sidelobes. In Planck Collaboration V (2016) we provide an overall upper limit based on the consistency of power spectra derived from different radiometers.

We are currently evaluating ways to improve this assessment in the context of the next *Planck* release. One possibility would be to use Monte Carlo simulations to assess the impact on calibration of uncertainties in the beam far sidelobes.

2.3. Bandpass mismatch

Mismatch between the bandpasses of the two orthogonally-polarized arms of the LFI radiometers causes leakage of foreground total intensity into the polarization maps. The effect and our correction for it are described in section 11 of Planck Collaboration II (2016) and references therein. A point to note is that the correction is only applied to at an angular resolution of 1°, although appendix C of Planck Collaboration XXVI (2016) describes a special procedure for correcting point source photometry derived from the full resolution maps.

Residual discrepancies between the blind and model-driven estimates of the leakage are noted in Planck Collaboration II (2016), which imply that the small (typically < 1 %) mismatch corrections are not perfect. The estimated fractional uncertainty in these corrections is < 25 % at 70 GHz and < 3 % at 30 GHz; the discrepancies are significant only because they are driven by the intense foreground emission on the Galactic plane.

As detailed in Sect. 3.1, our cosmological analysis of polarization data is restricted to 46 % of the sky with the weakest foreground emission. Planck Collaboration XI (2016) demonstrates that in this region the bandpass correction has a negligible effect on the angular power spectrum and cosmological parameters derived from it, the optical depth to reionization, τ, and the power spectrum amplitude. The same applies to our upper limit on the tensor-to-scalar ratio, Consequently the impact of the *uncertainty* in the correction is also negligible for the cosmological results.

3. Assessing residual systematic effect uncertainties in maps and power spectra

In this section we describe our assessment of systematic effects in the LFI data, which is based on a two-steps approach.

The first is to simulate maps of each effect (see Table 2) and combine them into a *global* map that contains the sum of all the effects. We perform simulations for various time intervals, single surveys, individual years and full mission, and we use such simulations to produce a set of *difference maps*. For example, we construct global systematic effects year-difference maps as the sum of all systematic effects for one year subtracted from from the sum of all systematics from another year. We also compare the pseudo-spectra computed on the full-mission maps with the expected sky signal to assess the impact of the various effects. This step is described in Sect. 3.2.

The second is to calculate the same difference maps from flight data. We call these maps *null maps*, because they should contain only white noise, as the sky observed in the time intervals of each pair of maps is the same. Here we compare the null maps pseudo-spectra with the pseudo-spectra of the *global* systematic effects difference maps. Our objective, in this case, is to highlight any residuals in the pseudo-spectra obtained from flight data that are not accounted for by our simulations. This step is described in Sect. 3.3.

Table 2: List of the simulated systematic effects.

Optical effects . . .	Near sidelobes Pointing uncertainty Polarization angle uncertainty
Thermal effects . .	4 K stage temp. fluct. 20 K stage temp. fluct. 300 K stage temp. fluct.
Calib. dependent .	ADC non-linearity Calibration uncertainty
Electronics	1-Hz spikes Bias fluctuations

In all cases we compute pseudo-spectra using the HEALPix `anafast` code and correct for the fraction of observed sky. In other words, in all the power spectra of this work we have $C_\ell = C_{\ell,\mathrm{anafast}}/f_{\mathrm{sky}}$, where $C_{\ell,\mathrm{anafast}}$ is the power spectrum as obtained by the `anafast` code and f_{sky} is the fraction of observed sky.

In Sect. 3.1 we start by reviewing the masks applied in the calculation of the pseudo-spectra used in our assessment.

3.1. Masks

We have used three masks to compute the power spectra discussed in this paper , and we show them in the three panels of Fig. 5.

The first mask (top panel of Fig. 5) is used for total intensity maps of the systematic effects. It removes the Galactic plane and point sources. It is the "UT78" mask described in section 4.1 of Planck Collaboration IX (2016), obtained by combining the `Commander`, `SEVEM`, and `SMICA` confidence masks.

The second mask (middle panel of Fig. 5) is used for Q and U maps of the systematic effects. It removes about 54 % of the sky, cutting out a large portion of the Galactic plane and the Northern and Southern Spurs. We adopted this mask in the low-ℓ likelihood used to extract the reionization optical depth parameter, τ (see figure 3 in Planck Collaboration XI 2016). We chose to use the same mask in the assessment of systematic effect uncertainties in polarization.

The third mask (bottom panel of Fig. 5) is used in the null maps analysis at all frequencies both in temperature and polarization. We obtained this mask by combining the UPB77 30-GHz polarization mask (right panel of figure 1 in Planck Collaboration IX 2016) and the 30-GHz point source mask used for the 2013 release described in section 4 of Planck Collaboration XII (2014)[9].

[9] Because difference maps may contain unobserved pixels, in each null test we take the union between this mask and any set of unobserved pixels. For example, maps of single surveys do not cover the full sky, which requires us to combine the mask with the unobserved pixels in the null map.

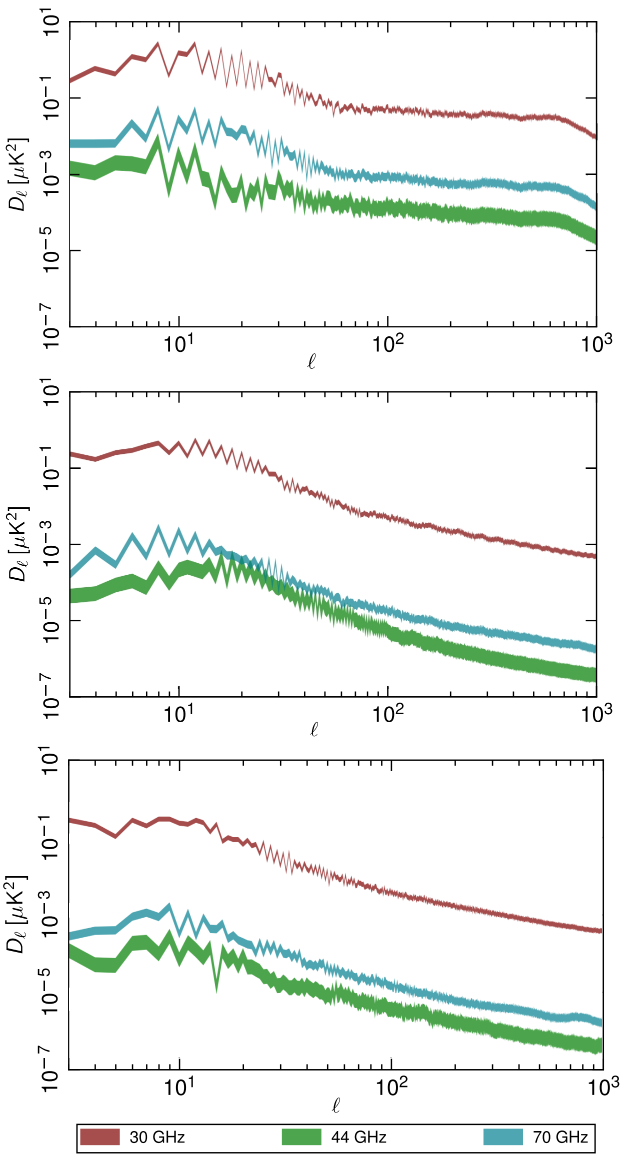

Fig. 6: Uncertainty in the power spectra of the effect from far sidelobes introduced by the first-order approximation in GRASP simulations. *Top: TT* spectrum. *Middle: EE* spectrum. *Bottom: BB* spectrum. For each frequency the coloured area is the region between the native power spectrum and the one rescaled to account for the missing power.

surveys are quite sensitive to the pickup of straylight by the far sidelobes and can be used to assess the presence of straylight residuals in the data. We discussed this point in Sect. 3.3.

We study the effect coming from the near sidelobes following the same procedure used for the far sidelobes. The main difference is that, in this case, we do not apply any correction to the data, so that our simulations estimate the systematic effect that we expect to be present in the data.

The maps in Fig. 8 show that near sidelobes especially impact measurements close to the Galactic plane. This is expected, because this region of the beam pattern is close to the main beam and causes a spurious signal when the beam scans regions of the sky with large brightness variations over small angular scales. This implies that near sidelobes do not significantly impact the recovery of the CMB power spectrum if the Galactic plane is properly masked. We confirm this through the power spectra, as shown in Figs. 24, 25, and 26.

Polarization angle. We study how the uncertainty in the polarization angle affects the recovered power spectra by means of a limited Monte Carlo exercise. We first produce a fiducial sky containing the CMB and foregrounds observed with the nominal polarization angles (Fig. 4) and then we generate five additional skies observed with a slightly different polarization angle for each feedhorn. Finally we compute the difference between each of the five maps and the fiducial sky.

In each of the five cases we rotate the polarization angle of each feed-horn by an amount equal to either the maximum or the minimum of the error bars shown in Fig. 4. In this way we can explore, for a small number of cases, a range of variability in the polarization angle that is larger compared to the range expected from the focal plane thermo-mechanical analysis.

The difference maps in Fig. 9 show that the effect is negligible in temperature (as expected) and is less than 1 μK at 70 GHz in polarization. At 30 and 44 GHz the maximum amplitude of the effect is around 2 μK and 1 μK, respectively. The maps shown represent one of the five cases picked randomly from the set.

In Figs. 10 and 11 we show the dispersion of the peak-to-peak and rms of this effect on maps, once we apply the masks in Fig. 5 (top one for total intensity and middle one for Q and U maps). The rms of the effect is smaller than 1 μK and also the dispersion introduced by the five different cases is small.

We observe that the peak-to-peak and rms of the effect in the polarization map decrease with frequency (see the bottom panels of Figs. 10 and 11). This correlates with the smaller contribution of polarized synchrotron emission in maps at higher frequency.

We also observe a higher residual at 44 GHz in temperature maps compared to the 30 and 70 GHz channels. We did not expect this behavior, and it is currently not understood. The effect in temperature, however, is much less than 0.1 μK and, therefore, completely negligible.

From the five sets of difference maps we have computed power spectra and evaluated their dispersion. We show the results in Fig. 12, where the grey area represents the region containing all the spectra and the blue curve is the average of these five spectra. The blue curve corresponds to the spectrum that is also reported in Figs. 24, 25, and 26.

Pointing. We have simulated the effect caused by pointing uncertainty by adding a Gaussian noise realization independently to both co-scan and cross-scan bore sight pointing. The noise realization was drawn from a $1/f$ noise model with a smooth cutoff at 10 mHz, which matches the single-planet transit analysis and

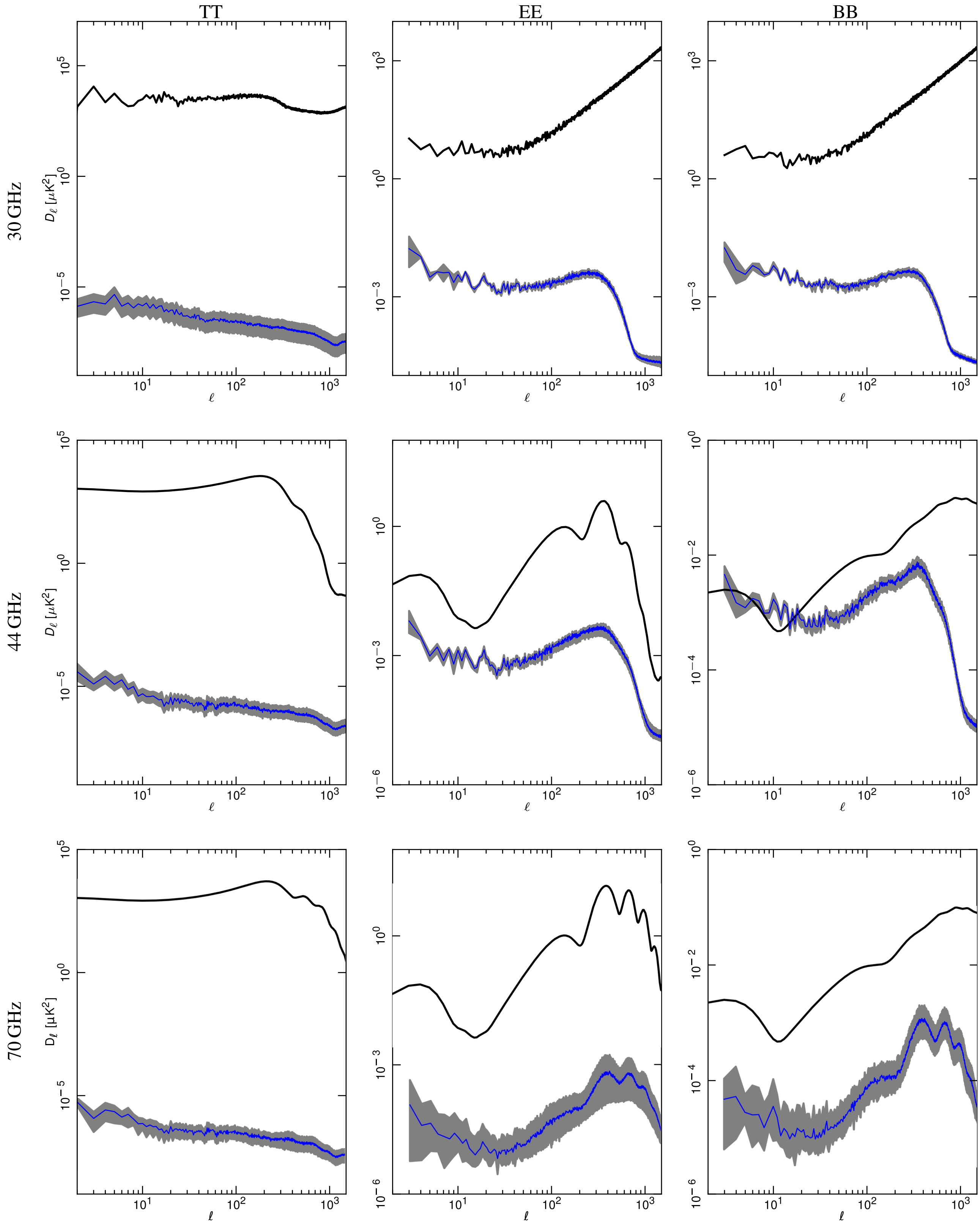

Fig. 12: Angular power spectra of the residual effect due to polarization angle uncertainty compared to the foreground spectra at 30 GHz and to *Planck* beam-filtered temperature and polarization spectra at 44 and 70 GHz. The blue curve represents the average spectrum, while the grey band is the envelope of all the power spectra calculated from the various realizations of the effect. The theoretical B-mode CMB spectrum assumes a tensor-to-scalar ratio $r = 0.1$, a tensor spectral index $n_{\mathrm{T}} = 0$ and has not been beam-filtered. Rows are for 30, 44, and 70 GHz spectra, while columns are for TT, EE and BB power spectra.

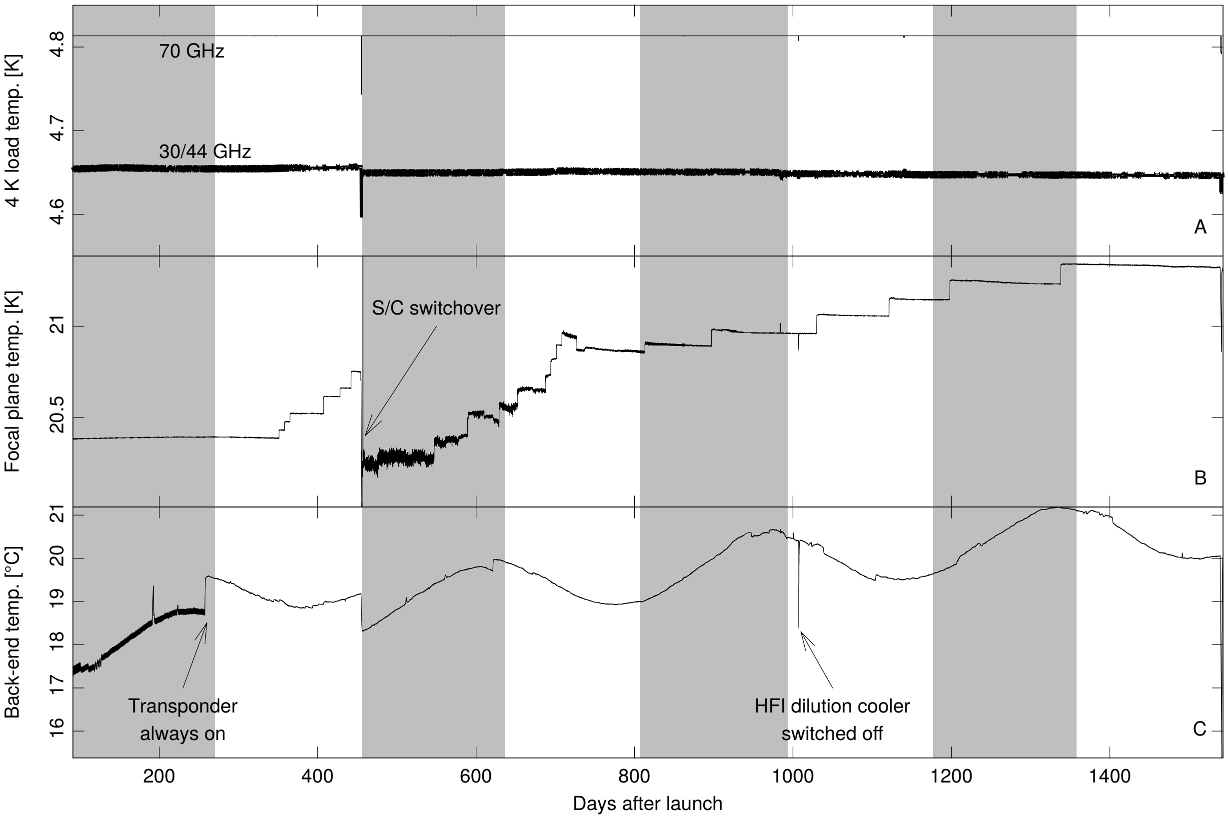

Fig. 16: *Top*: temperature measured by two sensors mounted on the HFI 4-K shield at the level of 30 and 44 GHz (bottom curve) and 70 GHz (top curve) reference loads. The rms variation of this temperature over the full mission is $\sigma_{30,44}$ = 1.55 mK and σ_{70} = 80 μK. *Middle*: temperature of the 20-K focal plane measured by a temperature sensor placed on the flange of the `LFI28` 30 GHz feedhorn. The consecutive temperature steps after day 500 reflect changes to the set-point of the temperature control system. We applied these changes to control the level of temperature fluctuations. *Bottom*: temperature of the 300-K back-end unit.

3.3.1. Null tests strategy

We complement every *Planck*-LFI data release with a suite of null tests combining data selected at various timescales.

The shortest timescale is that of a single pointing period (∼40 minutes) that is split into two parts. We then difference the corresponding maps and obtain the so-called *half-ring difference maps* that approximate the instrument noise and may contain systematic effects correlated on timescales $\lesssim$ 20 minutes.

Then we have longer timescales: six months (a sky survey), one year, the full mission (four years). We can create a large number of tests by combining these timescales for single radiometers[12]. We provide the detailed timing of each survey in the *Planck* Explanatory Supplement[13].

When we take a difference between two maps we apply a weighting to guarantee that we obtain the same level of white noise independently of the timescale considered. The weighting scheme is described by equations (30), (31), and (32) of Planck Collaboration II (2011), where we normalize the white noise to the full mission (8 surveys) noise. This means that in equation (32) of Planck Collaboration II (2011) the term $\mathbf{hit}_{\rm full}(p)$ corresponds to the number of hits at each pixel, p, in the full map.

We assess the quality of the null tests by comparing null maps pseudo spectra obtained from flight data with those coming from systematic effect simulations and with noise-only Monte Carlo realizations based on the *Planck full focal plane* (FFP8) simulation (Planck Collaboration XII 2016). For the systematic effect simulations we used *global* maps by combining the effects listed in Table 2. Monte Carlo realizations include pointing, flagging, and a radiometer specific noise model based on the measured noise power spectrum. We create 1000 random realizations of such noise maps using the same destriping algorithm used for the real data, and compute null maps and pseudo-spectra in the same way. For each multipole, ℓ, we calculate the mean C_ℓ and its dispersion by fitting the 1000 C_ℓs with an asymmetric Gaussian.

Passing these null tests is a strong indication of self-consistency. Of course, some effects could be present, at a certain level, in the various timescales, so that they are canceled out in the difference and remain undetected. However, the combined set of map differences allows us to gain confidence of our data and noise model.

[12] We do not expect that single radiometer survey differences are strictly null. Indeed, the radiometers are polarized detectors that observe the sky with a different range of polarization angles for different surveys. We use these tests to validate the radiometer stability, minimizing these effects by considering survey combinations with the same scanning patterns (survey 1 vs survey 3, survey 2 vs survey 4) or by combining radiometers to solve for I, Q and U.

[13] http://wiki.cosmos.esa.int/planckpla/index.php/Survey_scanning_and_performance

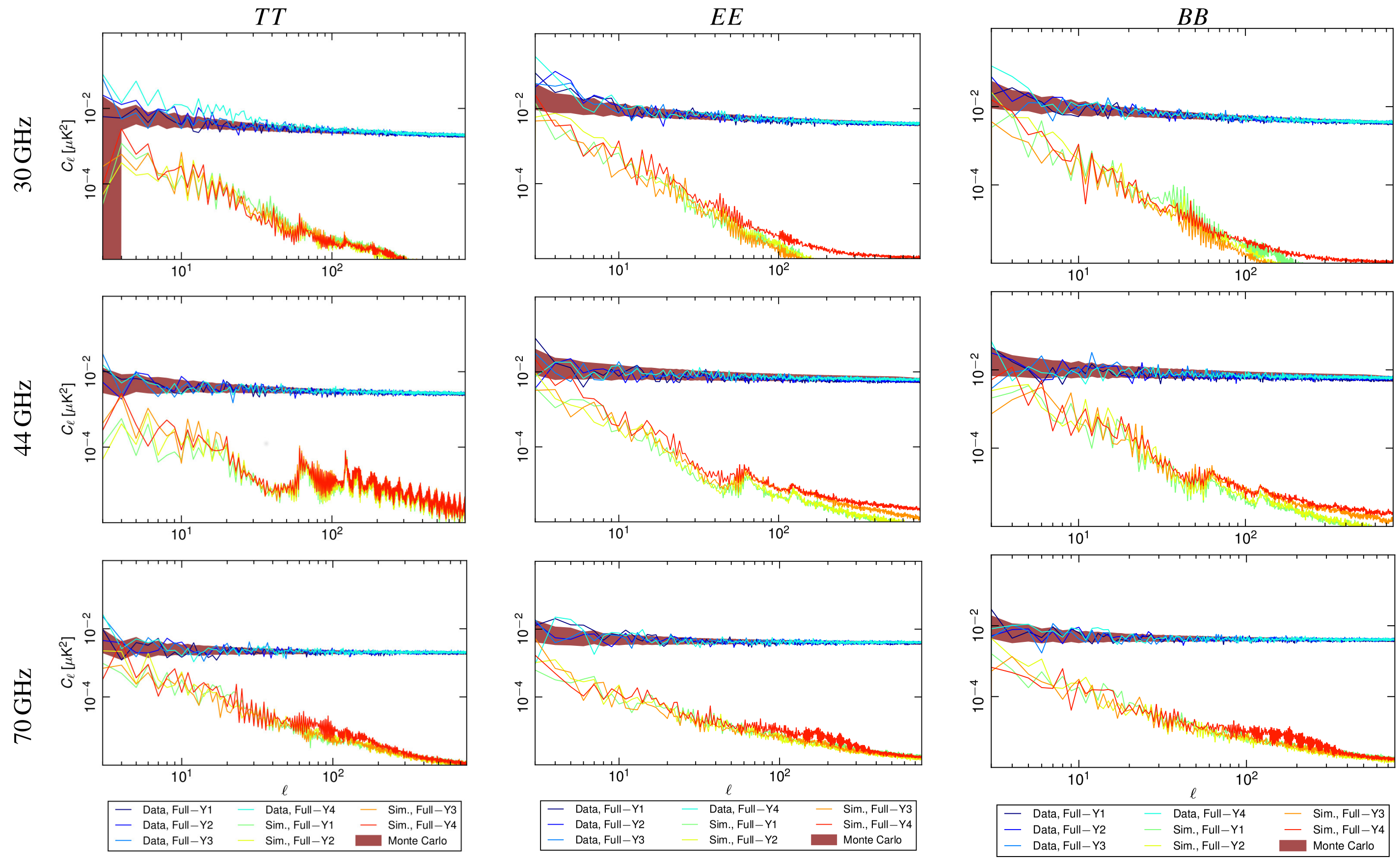

Fig. 20: Angular power spectra of *full* − *year* maps. Colored lines represent the four nulls obtained from data and simulations of the effects listed in Table 2. The purple colored area represents the envelope from Monte Carlo simulations as described in the text. In this figure we can appreciate that the power spectra of the data from the null maps are well matched by noise, except for a few low-ℓ points at 30 GHz. Furthermore, the power spectra of the simulated systematic effects fall well below the data at all but the lowest ℓ values.

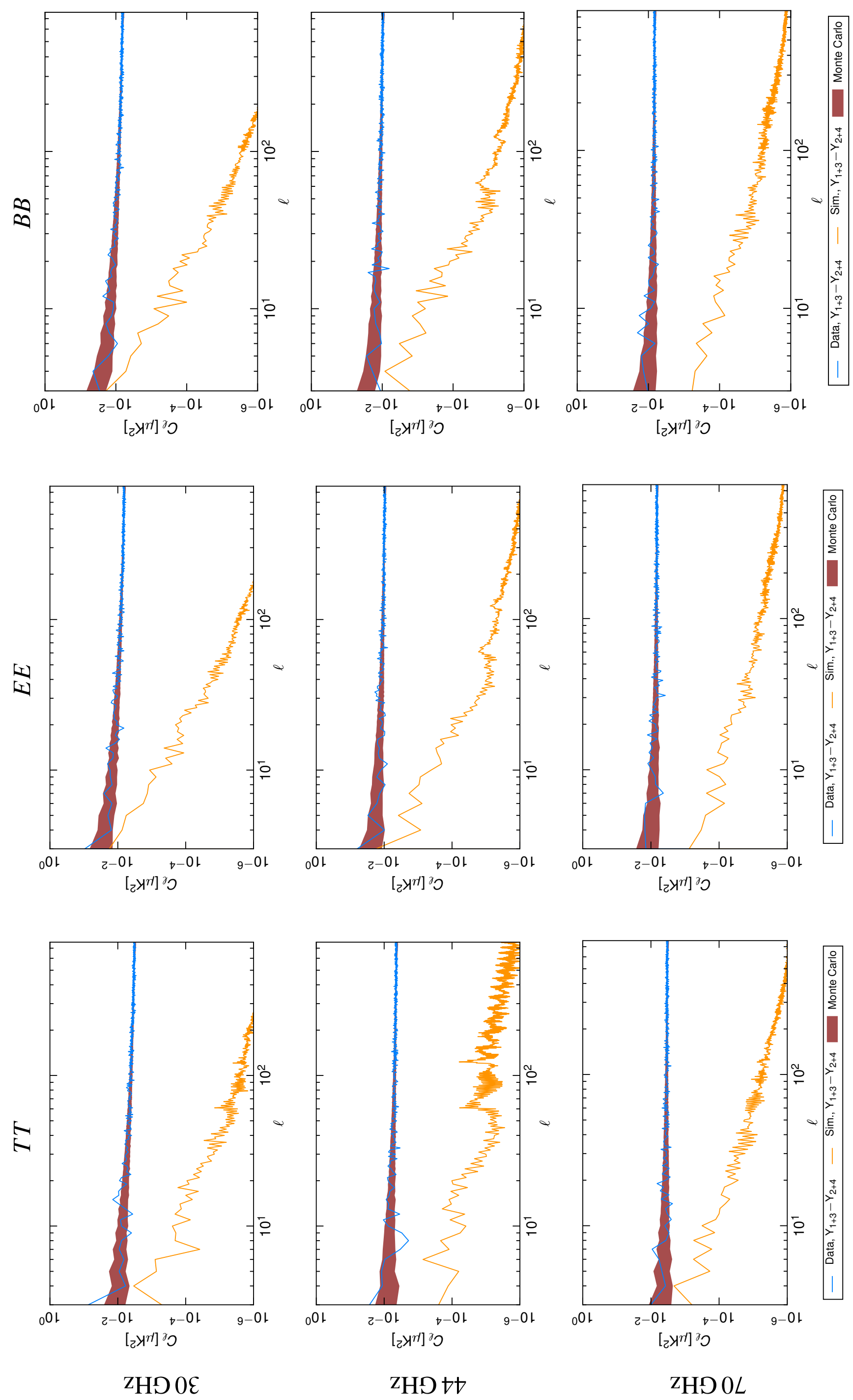

Fig. 21: Angular power spectra of *odd* – *even* year maps. Colored lines represent the four nulls obtained from data and simulations of the effects listed in Table 2. The colored area represents the envelope from Monte Carlo simulations as described in the text.

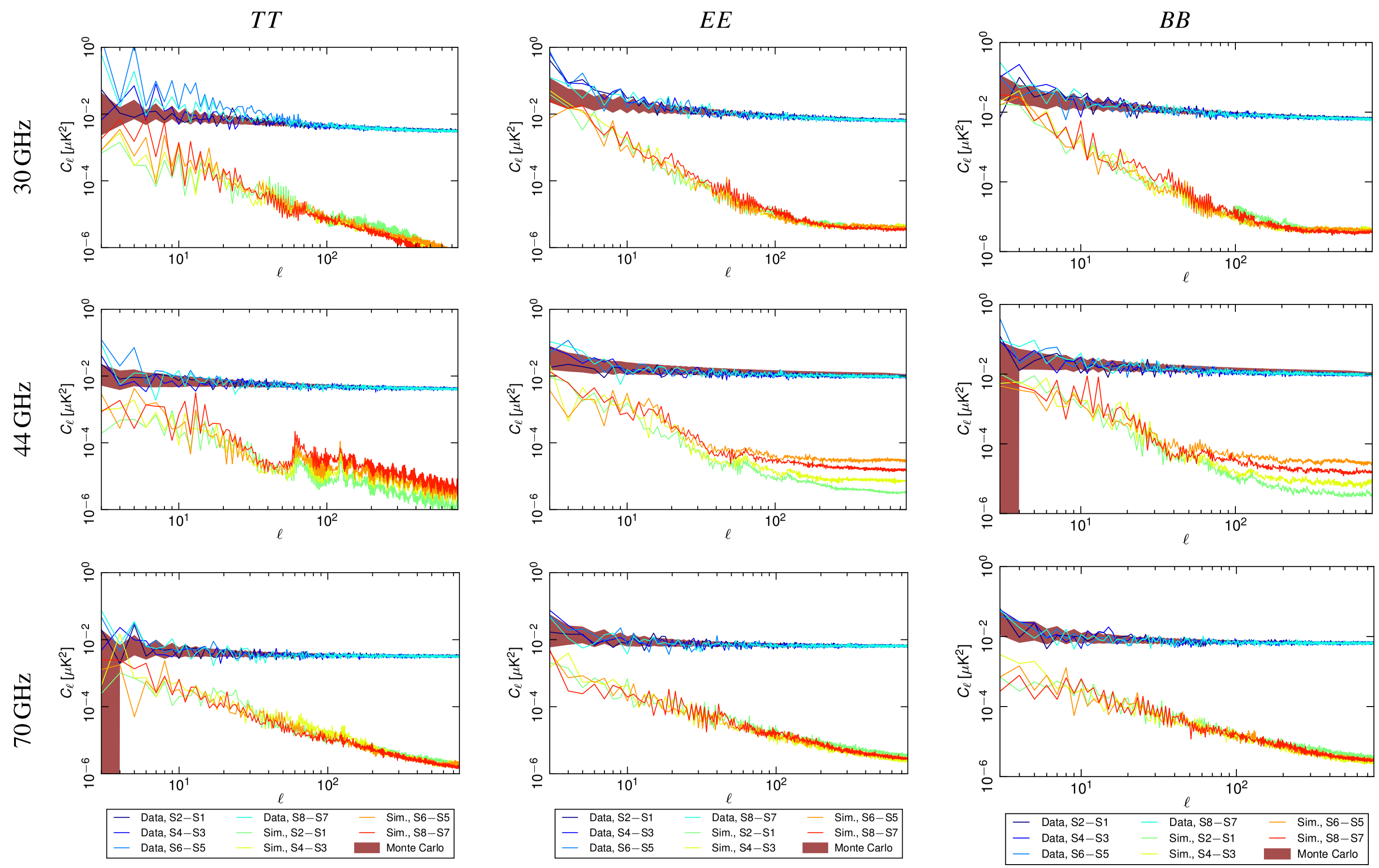

Fig. 22: Angular power spectra of consecutive survey difference maps. Colored lines represent the four nulls obtained from data and simulations of the effects listed in Table 2. The colored area represents the envelope from Monte Carlo simulations as described in the text.

ized distributions for each of the three parameters $X = \tau, r, A_s$ and calculate the differences $\Delta X = X_{\rm syst.} - X_{\rm no-syst.}$, which represent the bias introduced in the estimates of X by the combination of all systematic effects.

For $\log(A_{\rm s})$ and r we find median bias values of -0.026 and 0.11, respectively, which would correspond to a $0.2\,\sigma$ effect on the amplitude parameter and an increase of 15 % on the upper limit on r (95% CL). However, the dominant *Planck* constraints on these two parameters come effectively from temperature power spectrum at high multipoles, so the actual impact on the *Planck* results is very small.

For the optical depth, we find a mean bias $\langle\Delta\tau\rangle = 0.005$, or 0.2–0.25 times the standard deviation of the value of τ measured by LFI (Planck Collaboration XIII 2016). This result shows that the impact of all systematic effects on the measurement of τ is within 1σ. The measured $\langle\Delta\tau\rangle$ is compatible with a positive but sub-dominant bias by residual systematics, with an impact on τ well within the statistical uncertainty.

We emphasize that this result is based on our bottom-up approach, and therefore it relies on the accuracy and completeness of our model of all known instrumental systematic effects. As we have shown, at large angular scales systematics residuals from our model are only marginally dominated by the *EE* polarized CMB signal. For this reason we plan to produce a further independent tests on these data based both on null tests and on cross-spectra between the 70 GHz map and the HFI 100 and 143 GHz maps. Such a cross-instrument approach may prove particularly effective, because we expect that systematic effects between the two *Planck* instruments are largely uncorrelated. We will discuss these analyses in a forthcoming paper in combination with the release of the low-ell HFI polarization data at 100–217 GHz and in the final 2016 Planck release.

3.5. Propagation of systematic effects through component separation

In this section we discuss how we assess the impact of residual systematic effects in the LFI data on the CMB power spectra after component separation (see Fig. 27 in Sect. 4).

Planck component separation exploits a set of algorithms to derive each individual sky emission component. They are minimum variance in the needlet domain (`NILC`) or use foreground templates generally based on differences between two *Planck* maps that are close in frequency (`SEVEM`), as well as parametric fitting conducted in the pixel (`Commander`) and harmonic (`SMICA`) domains. We describe them in detail in Planck Collaboration IX (2016).

To assess residuals after component separation we use LFI systematic effect maps as the input for a given algorithm, setting the HFI channels to zero. This means that the output represents only the LFI systematic uncertainty in the corresponding CMB reconstruction. In Planck Collaboration III (2014) we exploited a global minimum-variance component-separation implementation, `AltICA`, to derive weights used to combine the LFI systematic effect maps. Here we generalize the same procedure using `NILC` and `SEVEM`. Both are based on minimum-variance estimation of the weights, but in localized spatial and harmonic domains, and so optimally subtract foregrounds where they are most relevant (`NILC`), and exploit foreground templates generally constructed by diffferencing two nearby *Planck* frequency channels (`SEVEM`).

Fig. 23 shows maps in total intensity and polarization of the LFI systematic effects after component separation. Maps extracted with `NILC` appear in the top row, while maps extracted with `SEVEM` appear in the bottom row. The structures that are most prominent outside the Galactic residuals appear to be associated with the scan strategy. Residuals are about 5 times larger for `NILC` than for `SEVEM`, for the reasons described in Sect. 4. It is important to stress that component separation does not alter the relative strength of the various systmatic effects treated in this paper, but simply filters them through the given foreground-cleaning pipeline.

Fig. 27 in Sect. 4 shows power spectra obtained from these maps compared with the best-fit *Planck* 2015 ΛCDM cosmology. To calculate these spectra we have first applied the masks shown in Fig. 5 and then computed pseudo-spectra corrected for the unseen sky fraction.

In total intensity we confirm the results presented in Planck Collaboration III (2014): the impact of known LFI systematic effects is at least two orders of magnitude less than the CMB. In polarization we observe a different residual level, depending on the algorithm used. The weighting strategy of `NILC` at large angular scales performed in the needlet domain yields a residual effect that is larger by about 1.5 orders of magnitude compared to `SEVEM`. We further discuss this discrepancy in Sect. 4. The 70-GHz channel is one with less foreground contamination and higher angular resolution. Hence, `NILC` weights this channel more compared to the others. This ultimately causes a larger level of residual systematic effects.

The residual effect in polarization after processing with `NILC` is comparable to interesting levels of cosmological *B*-modes at large scales. This particular point needs further attention for the next *Planck* data release, where component-separation solutions will be relevant for characterizing polarization accurately at large angular scales.

3.6. Gaussianity statitical tests

In this section we present the results of statistical tests assessing the impact of known systematic effects in the LFI data on non-Gaussianity studies.

The presence of systematic effect residuals can bias the statistical isotropy properties of the *Planck* maps (Planck Collaboration XVI 2016) or the constraints on primordial non-Gaussianity (Planck Collaboration XVII 2016). Therefore it is important to understand the impact of known systematic effects on the most relevant non-Gaussianity studies carried out within this release.

In the *Planck* 2013 release the non-Gaussianity studies were carried out using temperature data in two steps (Planck Collaboration III 2014). Firstly, we estimated an upper limit on the "detectability level" of all the known effects summed into a single "global" map. This level was defined as the factor we must multiply the global map by to generate a significant non-Gaussian deviation. Secondly, we measured the bias that these systematic effects could introduce on the local nonlinear coupling $f_{\rm NL}$ parameter.

In the current release we follow the same approach, considering, additionally, the polarization signal at low ℓ. We have also considered the three usual cases (namely local, equilateral, and orthogonal) for the bispectrum shape when defining $f_{\rm NL}$.

We characterize the level of detectability of the non-Gaussian contamination by comparing simulations that contain the systematic effect map added and rescaled by a global factor, $f_{\rm sys}$, with the null hypothesis (i.e., no systematic effects). We consider two scenarios, measuring the level of detectability of the systematic effects over: (i) the CMB + noise background;

ues measured in maps with and without systematic effects, i.e., $\Delta f_{\rm NL} \equiv f_{\rm NL}^{\rm sys} - f_{\rm NL}^{\rm clean}$.

To obtain a limit on this bias, we have first computed the full-sky bispectrum of the global systematic effect maps, following the formalism of Komatsu et al. (2002), and then we have cross-correlated it with the primordial bispectrum. We removed the bias generated by extragalactic point sources or the CIB-lensing, following the procedure described, e.g., in Curto et al. (2013, 2014).

Table 4 shows the values of the bias $\Delta f_{\rm NL}$ calculated at high resolution ($\ell_{\rm max}$ = 1024) for the LFI channels. The bias is normalized to the corresponding dispersion of $f_{\rm NL}$ to estimate the relative impact on the measurement of this parameter. For the three LFI channels, the impact of systematic effects on $f_{\rm NL}$ is negligible, being lower than 0.90 % for the local shape, 1.80 % for the equilateral shape and 2.22 % for the orthogonal shape. The 30 GHz channel has the highest amplitude for this bias, whereas the 44 and 70 GHz channels have maximum amplitudes of 0.02 % and 0.03 %, respectively.

4. Summary of uncertainties due to systematic effects

This section provides a top-level overview of the residual[15] uncertainties in the *Planck*-LFI CMB maps and power spectra, introduced by systematic effects. We list these effects in Table 1 and summarize the main results of our analysis, which are discussed in Sect. 3 and corresponding subsections.

Tables 5, 6, and 7 report the peak-to-peak[16] and rms systematic effect uncertainties in LFI maps. To calculate these uncertainties we have used `HEALPix` (Górski et al. 2005) maps with simulated systematic effects degraded to $N_{\rm side}$ = 128 (corresponding to a pixel size of around 28′) at 30 and 44 GHz, and $N_{\rm side}$ = 256 (corresponding to a pixel size of about 14′) at 70 GHz. This pixel sizes approximate the optical beam angular resolution. Maps were masked with the top and middle masks shown in Fig. 5, also used for power spectra estimation.

The rms uncertainty in LFI maps from known systematic effects is $\lesssim 0.5\,\mu$K in polarization and $\lesssim 1\,\mu$K in temperature. The improvements[17] introduced into the LFI pipeline have allowed us to reduce the peak-to-peak uncertainty by a factor ranging from 3.5 at 70 GHz to 7.7 at 30 GHz, compared to the 2013 analysis (Planck Collaboration III 2014). At 30 and 70 GHz calibration and analogue-to-digital converter (ADC) nonlinearity are the prevailing effects, while at 44 GHz calibration and 1-Hz spikes dominate.

In our assessment we have not included the residual effects from far sidelobes, because we remove Galactic straylight directly from the timelines. This removal is based on optical simulations, which implies that a residual effect may be present in the data. Estimating this remaining signal is complex and computationally demanding, since it requires us to generate Monte Carlo simulations of the far sidelobes. For the present analysis we have used the following approach regarding far sidelobes: we have assessed the impact of systematic effects assuming the perfect removal of Galactic straylight; and additionally we have quantified how much the far sidelobes would affect our results if they were not removed at all.

Figures 24, 25, and 26 provide an overview of the power spectra in temperature and polarization for each systematic effect, compared to the foreground levels at 30 GHz and to the cosmological signal at 44 and 70 GHz. At 30 GHz we use the spectrum obtained from measured data as an approximation of the foreground spectrum at this frequency. At 44 and 70 GHz we use the power spectrum coming from the best fits to the *Planck* cosmological parameters (see figures 9 and 10 in Planck Collab-

Table 5: Summary of systematic effect uncertainties on 30 GHz maps[a] in μK$_{\rm CMB}$. Columns give the peak-to-peak ("p-p") and rms levels for Stokes I, Q, and U maps.

	I		Q		U	
	p-p	rms	p-p	rms	p-p	rms
Near sidelobes	0.72	0.13	0.05	0.01	0.05	0.01
Pointing	0.37	0.07	0.02	0.01	0.02	0.00
Polarization angle	0.02	0.00	0.53	0.11	0.64	0.15
1-Hz spikes	0.54	0.11	0.11	0.02	0.09	0.02
Bias fluctuations	0.07	0.01	0.07	0.01	0.06	0.01
ADC nonlinearity	0.42	0.09	0.54	0.11	0.56	0.11
Calibration	2.43	0.55	2.53	0.46	2.34	0.43
Thermal fluct. (300 K)	0.00	0.00	0.00	0.00	0.00	0.00
Thermal fluct. (20 K)	0.12	0.03	0.06	0.02	0.06	0.02
Thermal fluct. (4 K)	0.29	0.06	0.06	0.01	0.05	0.01
Total[b]	2.72	0.61	2.79	0.52	2.42	0.49

[a] Calculated for a pixel size approximately equal to the average beam FWHM. A null value indicates a residual $< 10^{-2}\,\mu$K$_{\rm CMB}$.
[b] The total has been computed on maps resulting from the sum of individual systematic effect maps.

Table 6: Summary of systematic effect uncertainties on 44 GHz maps in μK$_{\rm CMB}$. Columns give the peak-to-peak ("p-p") and rms levels for Stokes I, Q, and U maps.

	I		Q		U	
	p-p	rms	p-p	rms	p-p	rms
Near sidelobes	0.09	0.02	0.00	0.00	0.00	0.00
Pointing	0.30	0.06	0.01	0.00	0.01	0.00
Polarization angle	0.04	0.01	0.35	0.07	0.38	0.10
1-Hz spikes	1.99	0.40	0.88	0.18	1.04	0.21
Bias fluctuations	0.04	0.01	0.05	0.01	0.05	0.01
ADC nonlinearity	0.30	0.06	0.36	0.07	0.34	0.07
Calibration	1.05	0.18	1.57	0.29	1.31	0.26
Thermal fluct. (300 K)	0.00	0.00	0.00	0.00	0.00	0.00
Thermal fluct. (20 K)	0.04	0.02	0.06	0.01	0.05	0.01
Thermal fluct. (4 K)	0.23	0.05	0.05	0.01	0.06	0.01
Total	2.29	0.45	1.95	0.37	1.76	0.37

[15] We use the word "residual" to refer to the spurious signal remaining in the final LFI maps due to a systematic effect, that is after any removal steps applied by the data analysis pipeline.
[16] In this paper we call "peak-to-peak" the difference between the 99% and the 1% quantiles of the pixel value distributions.
[17] See Sects. 4, 6, and 7 of Planck Collaboration II (2016)

Table 7: Summary of systematic effect uncertainties on 70 GHz maps in μK_{CMB}. Columns give the peak-to-peak (“p-p”) and rms levels for Stokes I, Q, and U maps.

	I		Q		U	
	p-p	rms	p-p	rms	p-p	rms
Near sidelobes	0.30	0.07	0.01	0.00	0.01	0.00
Pointing	0.60	0.11	0.03	0.01	0.03	0.01
Polarization angle	0.02	0.00	0.08	0.02	0.08	0.02
1-Hz spikes	0.39	0.08	0.17	0.03	0.15	0.03
Bias fluctuations	0.68	0.14	0.84	0.17	0.95	0.18
ADC nonlinearity	1.56	0.33	1.92	0.39	2.05	0.41
Calibration	1.06	0.23	0.98	0.18	0.77	0.16
Thermal fluct. (300 K)	0.00	0.00	0.00	0.00	0.00	0.00
Thermal fluct. (20 K)	0.44	0.08	0.07	0.01	0.08	0.02
Thermal fluct. (4 K)	0.38	0.08	0.04	0.01	0.05	0.01
Total	2.24	0.47	2.27	0.46	2.38	0.48

oration I 2016) filtered by the LFI window functions. The example CMB B-mode spectrum is based on *Planck*-derived cosmological parameters and assumes a tensor-to-scalar ratio $r = 0.1$, a tensor spectral index $n_T = 0$, and no beam-filtering. Instrumental noise here is based on “half-ring” difference maps, as described in sections 12.1 and 12.2 of Planck Collaboration II (2016).

In the same figure we also show the power spectra of Galactic straylight detected by the far sidelobes (the dotted green lines), which indicate the level of the effect that we expect to have removed from the data.

At 30 GHz the systematic effects are all lower than the foreground signal. The Galactic straylight is higher than the noise level at $\ell \lesssim 20$. For this reason we removed an estimate of Galactic straylight from the timelines, based on our best knowledge of the far sidelobes. These results show that the 30 GHz channel gives a reliable foreground template, with uncertainties set by the instrumental noise.

At 44 and 70 GHz the level of Galactic straylight is lower than the CMB. It is reasonable to assume that any residual that could be present in the data must be less than the total effect reported here and, therefore, negligible compared to the CMB.

The power spectrum of the sum of all systematic effects (dark-grey line) is higher than the E-mode spectrum in the ℓ range 10–15 and is marginally below that for multipoles < 10, at both 44 and 70 GHz. This could have an impact on the extraction of the optical depth, τ, which is strongly dependent on the C_ℓ^{EE} spectrum at very low ℓs.

We have evaluated the impact of the simulated effects on τ (see Sect. 3.4) and found a bias that is about 0.2 times the standard deviation, showing that the uncertainty on this parameter is dominated by statistics and the contribution from systematic effects is only of marginal importance.

We have also assessed the uncertainty caused by LFI systematic effects on the CMB power spectra estimated by *Planck* after component separation.

In our procedure (described in Sect. 3.5) we set the HFI channels to zero to evaluate the systematic uncertainty of LFI only in the CMB reconstruction. It is a generalization of the approach described in Planck Collaboration III (2014), based on component-separation weights calculated via minimum variance over the whole sky area considered. In this test we first input maps with the sum of all systematic effects into the component separation pipeline, then we apply the top and middle mask in Fig. 5 to the resulting maps and, finally, we calculate the pseudo-spectra.

Figure 27 shows the angular power spectra of the sum of all known LFI systematic effects in the component-separation outputs of the `NILC` and `SEVEM` algorithms described in Planck Collaboration IX (2016). These plots highlight the level of the residual effects compared with the *Planck* 2015 best-fit cosmology.

The results in total intensity confirm the findings of our previous data release. The residual systematic effects are several orders of magnitude lower than the CMB power spectrum at all angular scales.

The results in polarization show that the residual effects resulting after the application of the `SEVEM` algorithm are about 1.5–2 orders of magnitude lower than those resulting from `NILC`, at all angular scales. This means that the residual effects obtained with `NILC` have an amplitude comparable to cosmological B-modes with $r \sim 0.1$.

The reason for this discrepancy in the component-separated outputs is the different weighting that the two codes apply to the LFI channels. In `NILC` the LFI channels are weighted more than in `SEVEM`, which also implies a larger impact of the systematic effects. Let us recall the reasons for this different weighting.

`NILC` implements a minimum variance approach in the needlet domain, and produces a set of weights for each ℓ-band in which it is applied. For this reason, in the LFI channels the weights are particularly relevant at large angular scales, where foregrounds are most important.

`SEVEM`, on the other hand, applies a smoothing to the LFI channels and then calculates the minimum variance coefficients over the entire range of multipoles, which eventually results in smaller weights for the LFI channels and, therefore, a smaller contribution of their systematic effects.

5. Conclusions

This is the era of precision cosmology. The advances in detector and space technology in the last 20 years now allow us to test theories describing the evolution of the Universe with statistical uncertainties that were unimaginable at the time the CMB was discovered, more than 50 years ago.

Planck has produced the most sensitive full-sky maps of the microwave sky to date. We have exploited its unprecedented statistical power to obtain the most precise angular temperature power spectrum of the CMB (Planck Collaboration XI 2016), as well as cosmological parameters with relative errors below the percent level in some cases (Planck Collaboration XIII 2016).

In the last ten years several experiments from the ground and the stratosphere have successfully tested new technologies that are further increasing sensitivity and opening new frontiers for cosmology by exploiting measurements of the CMB anisotropy polarization.

However, precision is nothing without accuracy. Understanding and controlling systematic uncertainties is one of the greatest challenges for present and future measurements of the CMB. The control of systematic effects has indeed been a challenge for *Planck*, both in the development phase and during data analysis.

In this paper we have discussed the systematic effect uncertainties of the *Planck* Low Frequency Instrument data in the con-

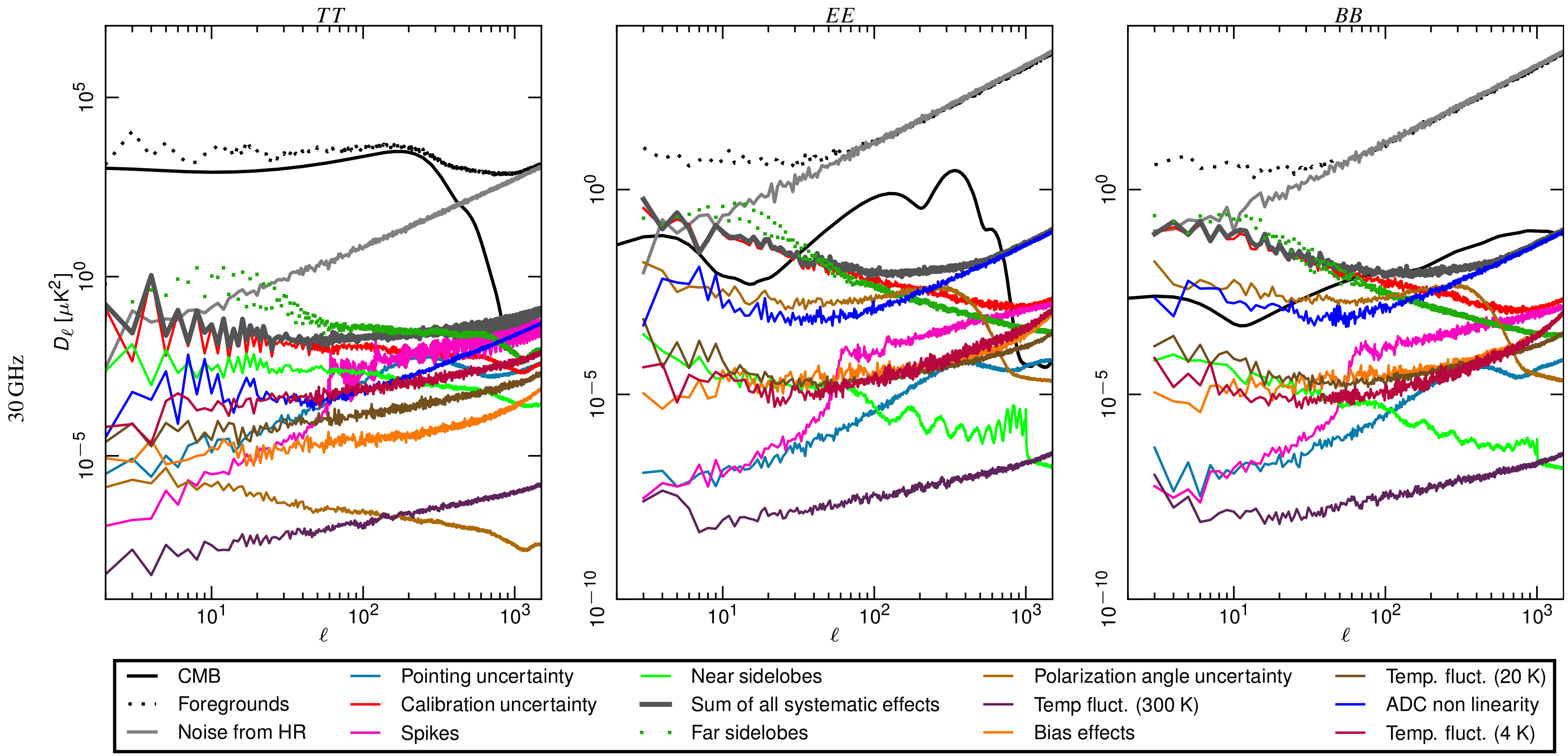

Fig. 24: Angular power spectra of the various systematic effects at 30 GHz, compared to the CMB and foreground temperature and polarization spectra and to the instrumental noise from half-ring (HR) difference maps. The CMB TT and EE spectra are best fits to the *Planck* cosmological parameters (see figures 9 and 10 in Planck Collaboration I 2016) filtered by the LFI window functions. The example CMB B-mode spectrum is based on *Planck*-derived cosmological parameters and assumes a tensor-to-scalar ratio $r = 0.1$, a tensor spectral index $n_{\mathrm{T}} = 0$, and no beam-filtering. The thick dark-grey line represents the total contribution. The dotted dark-green line is the contribution from the far sidelobes that has been removed from the data and is therefore not considered in the total.

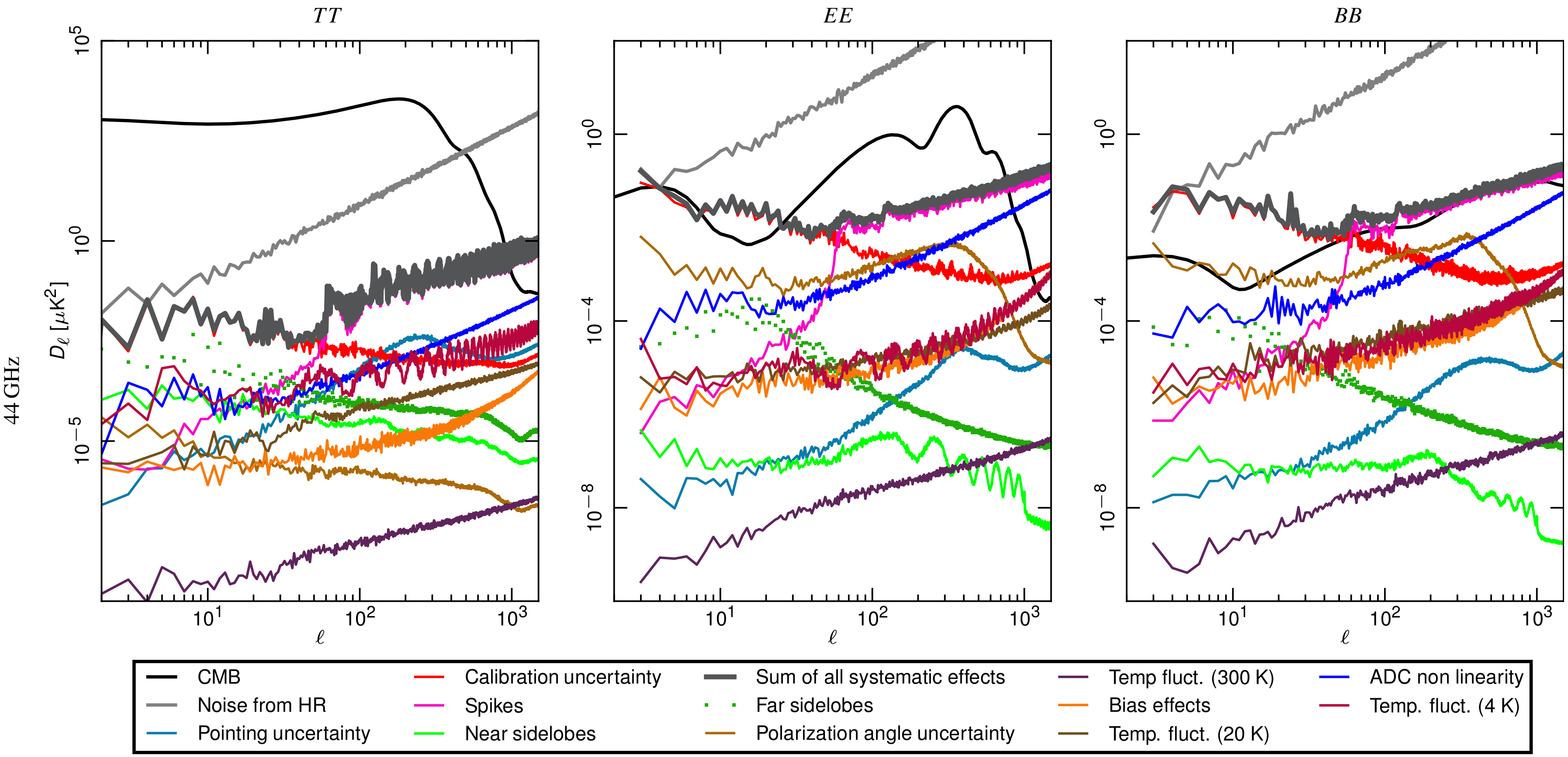

Fig. 25: Angular power spectra of the various systematic effects at 44 GHz, compared to the CMB temperature and polarization spectra and to the instrumental noise from half-ring (HR) difference maps. The CMB TT and EE spectra are best fits to the *Planck* cosmological parameters (see figures 9 and 10 in Planck Collaboration I 2016) filtered by the LFI window functions. The example CMB B-mode spectrum is based on *Planck*-derived cosmological parameters and assumes a tensor-to-scalar ratio $r = 0.1$, a tensor spectral index $n_{\rm T} = 0$, and no beam-filtering. The thick dark-grey line represents the total contribution. The dotted dark-green line is the contribution from far the sidelobes that has been removed from the data and is therefore not considered in the total.

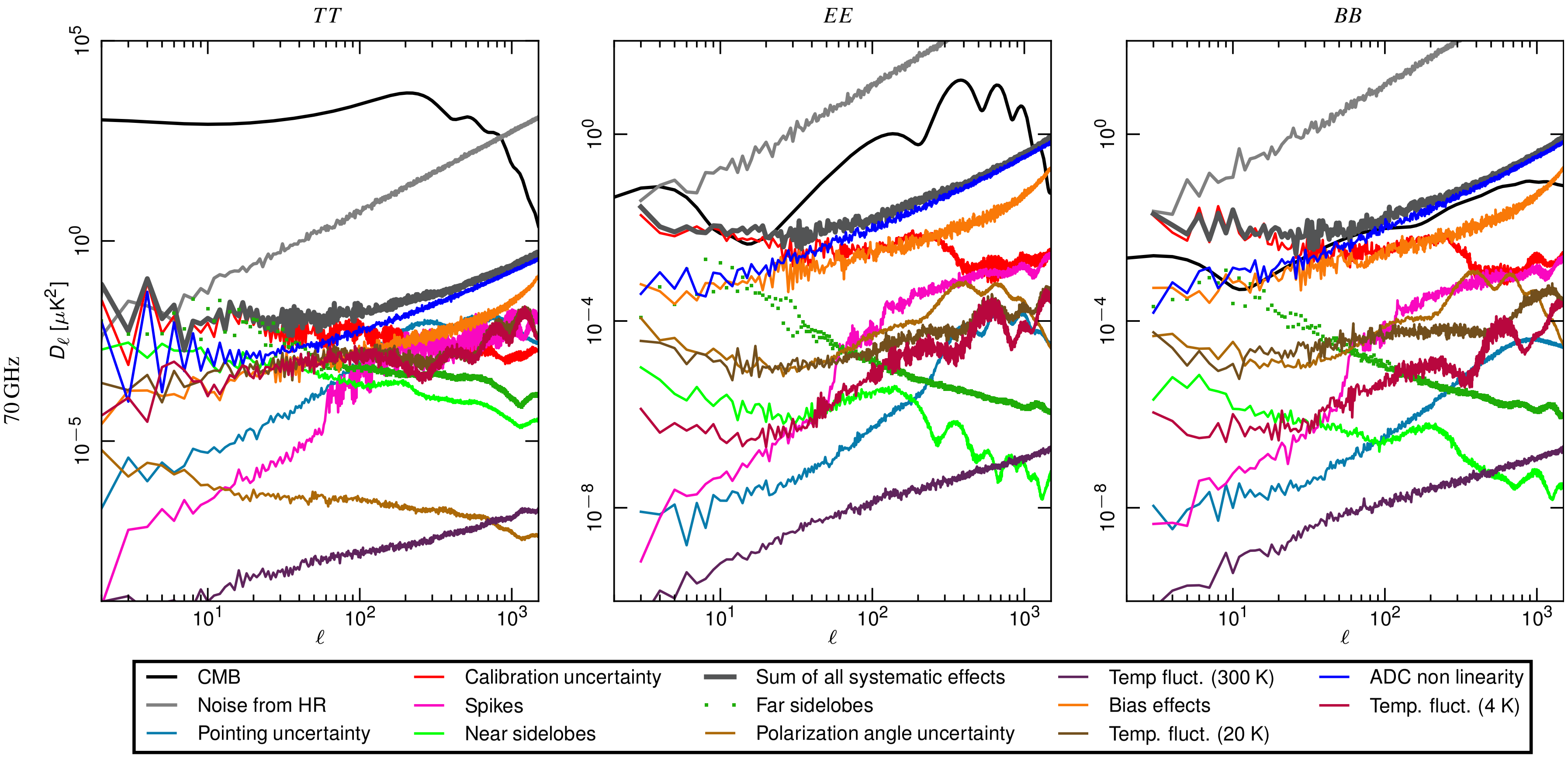

Fig. 26: Angular power spectra of the various systematic effects at 70 GHz, compared to the CMB temperature and polarization spectra and to the instrumental noise from half-ring (HR) difference maps. The CMB TT and EE spectra are best fits to the *Planck* cosmological parameters (see figures 9 and 10 in Planck Collaboration I 2016) filtered by the LFI window functions. The example CMB B-mode spectrum is based on *Planck*-derived cosmological parameters and assumes a tensor-to-scalar ratio $r = 0.1$, a tensor spectral index $n_\mathrm{T} = 0$, and no beam-filtering. The thick dark-grey line represents the total contribution. The dotted dark-green line is the contribution from far the sidelobes that has been removed from the data and is therefore not considered in the total.

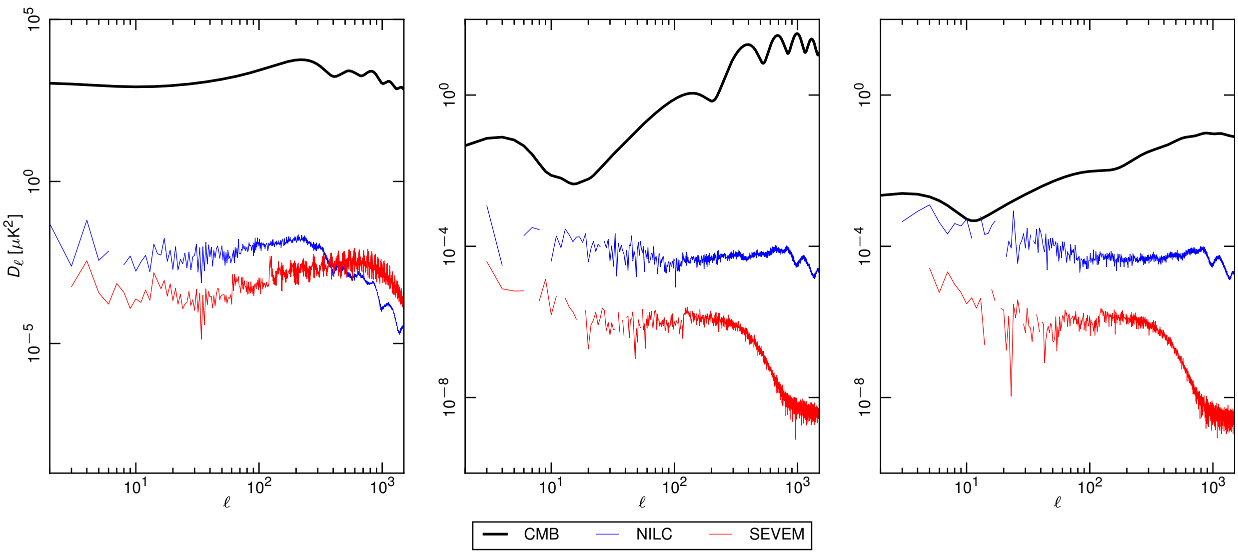

Fig. 27: Angular power spectra for the combined LFI systematic effects templates in the CMB TT, EE, and BB reconstructions of the `NILC` and `SEVEM` pipelines, compared with the *Planck* fiducial cosmology.

text of the second cosmological data release. This is the result of work begun almost 20 years ago, when we started developing the instrument with systematic effects control as one of the main drivers for the instrument and data-analysis pipeline designs.

Our approach follows two complementary paths.

- The first uses measured data and exploits the redundancy in the scanning strategy to divide the observations into periods of various length in which the observed sky is the same. We used the analysis of difference maps constructed on such periods ("null tests") to highlight possible spurious residual signals exceeding the instrumental noise.
- the second uses our knowledge of the instrument to build physical models of the various known systematic effects that are simulated from timelines to maps. Here we exploit, as much as possible, actual flight measurements, such as pointing, temperatures, and radiometric data.

We use simulations to quantify the uncertainties introduced by systematic effects in the maps and power spectra, and compare our predictions with null-test results to identify residuals that are not accounted for by our model. We also use our simulations to assess the impact of these effects on cosmological parameters (like the reionization optical depth, τ) on the measurements of the CMB statistical properties, and on component separation.

Our results for temperature data confirm the findings of the first *Planck* release (Planck Collaboration III 2014): the measurements are limited by instrumental noise and at all relevant angular scales the systematic effects are several orders of magnitude below the power spectrum of the CMB itself.

Our analysis for polarization demonstrates the robustness of the LFI data for scientific analysis, in particular regarding the measurement of τ and the statistical analysis of CMB maps. Systematic effects, however, are more challenging in polarization than in temperature and their level is close to the E-mode signal, especially at large angular scales.

Uncertainties in the relative photometric calibrations dominate the LFI systematic effects budget, especially at large angular scales. This is an area in the data analysis pipeline that is still being improved in preparation for the next *Planck* release.

Our data could also contain residual Galactic straylight caused by an imperfect knowledge of the beam sidelobes. We do not consider this residual in our budget, but null spectra from consecutive surveys indicate a possible presence of such a spurious signal at 30 GHz.

At 70 GHz the systematic effects compete with the CMB E-modes for multipoles in the range 10–20. This does not preclude an accurate measurement of τ, which depends mainly on multipoles $\ell < 10$ (Planck Collaboration XI 2016). Using systematic effects simulations we have shown that the bias introduced on τ is less than 0.25 times the standard deviation of the measured parameter. Forthcoming analyses will include independent estimations, based on null tests and on cross-correlation between the LFI 70 GHz map and the HFI 100 and 143 GHz maps.

We have also evaluated the impact on the scalar perturbations amplitude, $\ln(A_s)$, and on the upper limit to the tensor-to-scalar ratio, r, derived with large-scale polarization data. In this case the effect on $\ln(A_s)$ is approximately $0.2\,\sigma$, while the upper limit on r is increased by the systematic effects by around 15 %. For these two parameters, however, the main *Planck* constraint comes from the temperature power spectrum at high multipoles, so that the actual impact is negligible.

At 30 GHz the systematic effects are much smaller than the Galactic emission at all multipoles. We use this channel as a foreground monitor, which implies that we are not limited by systematic effects at this frequency for any angular scale, in either temperature or polarization.

The 44 GHz channel displays residuals that compete with the E-mode polarization for $\ell \leq 10$ and dominate the signal for multipoles in the range 10–20. We do not use this channel in the current polarization analysis, so these effects do not play a role in the measurement of τ. We use the 44 GHz data, however, in the component separation analysis.

The contribution of LFI systematic effects on CMB maps and power spectra after component separation is smaller than the CMB signal at all scales, both in temperature and polarization. We have assessed this using two component separation codes, namely `NILC` (a minimum variance code in the needlet domain) and `SEVEM` (a code based on foreground templates). With both codes the LFI systematic uncertainties do not limit accurate measurement of the CMB temperature and polarization spectra. As expected, we find that the use of `SEVEM` results in a lower level of residuals compared to `NILC`, because of the different weighting of the LFI data applied by the two codes.

The presence of known systematic effects in the LFI data does not significantly impact non-Gaussianity studies. We have used maps with the simulated effects combined with CMB and noise maps and found that, at 70 GHz, the amplitude of these effects must be at least a factor of 2 larger to detect a significant non-Gaussianity. We have also assessed the bias on the $f_{\rm NL}$ parameter and found that it is less than 0.1 % at 44 and 70 GHz and < 2.2 % at 30 GHz.

Finally, we comment about the systematic uncertainties on the B-mode polarization measurements. Our analysis shows that at 70 GHz the level of systematic effects is smaller than the instrumental noise, but larger than a B-mode power spectrum for $r = 0.1$. This does not impact our polarization analysis, based on E-mode polarization data, but shows, once again, the importance of understanding and controlling systematic effects in future experiments aiming at the detection of this elusive signal.

Understanding and controlling systematic effects in the LFI data has been a challenge from which we have gained even deeper knowledge of our instrument and learned several valuable lessons for the future. This is a future destined to be one of even more precise and accurate cosmology, but also one of increasing challenge to control systematics effects,

Acknowledgements. The Planck Collaboration acknowledges the support of: ESA; CNES, and CNRS/INSU-IN2P3-INP (France); ASI, CNR, and INAF (Italy); NASA and DoE (USA); STFC and UKSA (UK); CSIC, MINECO, JA, and RES (Spain); Tekes, AoF, and CSC (Finland); DLR and MPG (Germany); CSA (Canada); DTU Space (Denmark); SER/SSO (Switzerland); RCN (Norway); SFI (Ireland); FCT/MCTES (Portugal); ERC and PRACE (EU). A description of the Planck Collaboration and a list of its members, indicating which technical or scientific activities they have been involved in, can be found at http://www.cosmos.esa.int/web/planck/planck_collaboration. Some of the results in this paper have been derived using the `HEALPix` package.

References

Aumont, J., Conversi, L., Thum, C., et al., Measurement of the Crab nebula polarization at 90 GHz as a calibrator for CMB experiments. 2010, A&A, 514, A70, 0912.1751

Bersanelli, M., Mandolesi, N., Butler, R. C., et al., *Planck* pre-launch status: Design and description of the Low Frequency Instrument. 2010, A&A, 520, A4, 1001.3321

Burigana, C., Sandri, M., Villa, F., et al., Trade-off between angular resolution and straylight contamination in the PLANCK Low Frequency Instrument (II Straylight evaluation). 2004, Astronomy & Astrophysics, 428, 311

Curto, A., Tucci, M., González-Nuevo, J., et al., Forecasts on the contamination induced by unresolved point sources in primordial non-Gaussianity beyond Planck. 2013, MNRAS, 432, 728, 1301.1544

Curto, A., Tucci, M., Kunz, M., & Martinez-Gonzalez, E., The CIB-lensing bispectrum: impact on primordial non-Gaussianity and detectability for the Planck mission. 2014, ArXiv e-prints, 1405.7029

Górski, K. M., Hivon, E., Banday, A. J., et al., HEALPix: A Framework for High-Resolution Discretization and Fast Analysis of Data Distributed on the Sphere. 2005, ApJ, 622, 759, astro-ph/0409513

Gregorio, A., Cuttaia, F., Mennella, A., et al., In-flight calibration and verification of the Planck-LFI instrument. 2013, Journal of Instrumentation, 8, 7001, 1307.2029

Hinshaw, G., Weiland, J. L., Hill, R. S., et al., Five-Year Wilkinson Microwave Anisotropy Probe (WMAP) Observations: Data Processing, Sky Maps, and Basic Results. 2009, ApJS, 180, 225, 0803.0732

Keihänen, E., Keskitalo, R., Kurki-Suonio, H., Poutanen, T., & Sirviö, A., Making cosmic microwave background temperature and polarization maps with MADAM. 2010, A&A, 510, A57, 0907.0367

Komatsu, E., Wandelt, B. D., Spergel, D. N., Banday, A. J., & Górski, K. M., Measurement of the Cosmic Microwave Background Bispectrum on the COBE DMR Sky Maps. 2002, ApJ, 566, 19, arXiv:astro-ph/0107605

Kurki-Suonio, H., Keihänen, E., Keskitalo, R., et al., Destriping CMB temperature and polarization maps. 2009, A&A, 506, 1511, 0904.3623

Lamarre, J., Puget, J., Ade, P. A. R., et al., *Planck* pre-launch status: The HFI instrument, from specification to actual performance. 2010, A&A, 520, A9

Leahy, J. P., Bersanelli, M., D'Arcangelo, O., et al., *Planck* pre-launch status: Expected LFI polarisation capability. 2010, A&A, 520, A8

Mennella, A., Bersanelli, M., Butler, R. C., et al., *Planck* pre-launch status: Low Frequency Instrument calibration and expected scientific performance. 2010, A&A, 520, A5, 1001.4562

Mennella, A., Butler, R. C., Curto, A., et al., *Planck* early results. III. First assessment of the Low Frequency Instrument in-flight performance. 2011, A&A, 536, A3, 1101.2038

Planck Collaboration ES. 2015, The Explanatory Supplement to the *Planck* 2015 results, http://wiki.cosmos.esa.int/planckpla/index.php/Main_Page (ESA)

Planck Collaboration II, *Planck* early results. II. The thermal performance of *Planck*. 2011, A&A, 536, A2, 1101.2023

Planck Collaboration I, *Planck* 2013 results. I. Overview of products and scientific results. 2014, A&A, 571, A1, 1303.5062

Planck Collaboration III, *Planck* 2013 results. III. LFI systematic uncertainties. 2014, A&A, 571, A3, 1303.5064

Planck Collaboration V, *Planck* 2013 results. V. LFI Calibration. 2014, A&A, 571, A5, 1303.5066

Planck Collaboration XII, *Planck* 2013 results. XII. Diffuse component separation. 2014, A&A, 571, A12, 1303.5072

Planck Collaboration I, *Planck* 2015 results. I. Overview of products and results. 2016, A&A, submitted, 1502.01582

Planck Collaboration II, *Planck* 2015 results. II. Low Frequency Instrument data processing. 2016, A&A, submitted, 1502.01583

Planck Collaboration III, *Planck* 2015 results. III. LFI systematic uncertainties. 2016, A&A, submitted, 1507.08853

Planck Collaboration IV, *Planck* 2015 results. IV. LFI beams and window functions. 2016, A&A, in press, 1502.01584

Planck Collaboration V, *Planck* 2015 results. V. LFI calibration. 2016, A&A, in press, 1505.08022

Planck Collaboration VI, *Planck* 2015 results. VI. LFI maps. 2016, A&A, submitted, 1502.01585

Planck Collaboration VII, *Planck* 2015 results. VII. High Frequency Instrument data processing: Time-ordered information and beam processing. 2016, A&A, in press, 1502.01586

Planck Collaboration VIII, *Planck* 2015 results. VIII. High Frequency Instrument data processing: Calibration and maps. 2016, A&A, in press, 1502.01587

Planck Collaboration IX, *Planck* 2015 results. IX. Diffuse component separation: CMB maps. 2016, A&A, submitted, 1502.05956

Planck Collaboration X, *Planck* 2015 results. X. Diffuse component separation: Foreground maps. 2016, A&A, submitted, 1502.01588

Planck Collaboration XI, *Planck* 2015 results. XI. CMB power spectra, likelihoods, and robustness of parameters. 2016, A&A, submitted, 1507.02704

Planck Collaboration XII, *Planck* 2015 results. XII. Full Focal Plane simulations. 2016, A&A, submitted, 1509.06348

Planck Collaboration XIII, *Planck* 2015 results. XIII. Cosmological parameters. 2016, A&A, submitted, 1502.01589

Planck Collaboration XIV, *Planck* 2015 results. XIV. Dark energy and modified gravity. 2016, A&A, submitted, 1502.01590

Planck Collaboration XV, *Planck* 2015 results. XV. Gravitational lensing. 2016, A&A, submitted, 1502.01591

Planck Collaboration XVI, *Planck* 2015 results. XVI. Isotropy and statistics of the CMB. 2016, A&A, in press, 1506.07135

Planck Collaboration XVII, *Planck* 2015 results. XVII. Constraints on primordial non-Gaussianity. 2016, A&A, submitted, 1502.01592

Planck Collaboration XVIII, *Planck* 2015 results. XVIII. Background geometry and topology of the Universe. 2016, A&A, submitted, 1502.01593

Planck Collaboration XIX, *Planck* 2015 results. XIX. Constraints on primordial magnetic fields. 2016, A&A, submitted, 1502.01594

Planck Collaboration XX, *Planck* 2015 results. XX. Constraints on inflation. 2016, A&A, submitted, 1502.02114

Planck Collaboration XXI, *Planck* 2015 results. XXI. The integrated Sachs-Wolfe effect. 2016, A&A, submitted, 1502.01595

Planck Collaboration XXII, *Planck* 2015 results. XXII. A map of the thermal Sunyaev-Zeldovich effect. 2016, A&A, submitted, 1502.01596

Planck Collaboration XXIII, *Planck* 2015 results. XXIII. The thermal Sunyaev-Zeldovich effect–cosmic infrared background correlation. 2016, A&A, submitted, 1509.06555

Planck Collaboration XXIV, *Planck* 2015 results. XXIV. Cosmology from Sunyaev-Zeldovich cluster counts. 2016, A&A, submitted, 1502.01597

Planck Collaboration XXV, *Planck* 2015 results. XXV. Diffuse, low-frequency Galactic foregrounds. 2016, A&A, submitted, 1506.06660
Planck Collaboration XXVI, *Planck* 2015 results. XXVI. The Second Planck Catalogue of Compact Sources. 2016, A&A, submitted, 1507.02058
Planck Collaboration XXVII, *Planck* 2015 results. XXVII. The Second Planck Catalogue of Sunyaev-Zeldovich Sources. 2016, A&A, in press, 1502.01598
Planck Collaboration XXVIII, *Planck* 2015 results. XXVIII. The Planck Catalogue of Galactic Cold Clumps. 2016, A&A, in press, 1502.01599
Reinecke, M., Dolag, K., Hell, R., Bartelmann, M., & Enßlin, T. A., A simulation pipeline for the Planck mission. 2006, A&A, 445, 373, astro-ph/0508522
Sandri, M., Villa, F., Bersanelli, M., et al., *Planck* pre-launch status: Low Frequency Instrument optics. 2010, A&A, 520, A7
Sandri, M., Villa, F., Nesti, R., et al., Trade-off between angular resolution and straylight contamination in the PLANCK Low Frequency Instrument (I pattern simulations). 2004, Astronomy & Astrophysics, 428, 299
Seiffert, M., Mennella, A., Burigana, C., et al., 1/f noise and other systematic effects in the Planck-LFI radiometers. 2002, A&A, 391, 1185, astro-ph/0206093
Terenzi, L., Salmon, M. J., Colin, A., et al., Thermal susceptibility of the Planck-LFI receivers. 2009, Journal of Instrumentation, 4, 2012, 1001.4653
TICRA Engineering Consultants. 2008, GRASP, technical descritpion (Knud Pontoppidan, TICRA, Denmark)
TICRA Engineering Consultants. 2012, GRASP Multi-GTD add-on (Knud Pontoppidan, TICRA, Denmark)
Tomasi, M., Cappellini, B., Gregorio, A., et al., Dynamic validation of the Planck-LFI thermal model. 2010, Journal of Instrumentation, 5, 1002, 1001.4646
Villa, F., Pagan, L., & Sandri, M. 2005, LFI alignment evaluation and recovery proposal, Tech. Rep. PL-LFI-PST-TN-054, LFI
Zacchei, A., Maino, D., Baccigalupi, C., et al., *Planck* early results. V. The Low Frequency Instrument data processing. 2011, A&A, 536, A5, 1101.2040

[1] APC, AstroParticule et Cosmologie, Université Paris Diderot, CNRS/IN2P3, CEA/lrfu, Observatoire de Paris, Sorbonne Paris Cité, 10, rue Alice Domon et Léonie Duquet, 75205 Paris Cedex 13, France
[2] African Institute for Mathematical Sciences, 6-8 Melrose Road, Muizenberg, Cape Town, South Africa
[3] Agenzia Spaziale Italiana Science Data Center, Via del Politecnico snc, 00133, Roma, Italy
[4] Aix Marseille Université, CNRS, LAM (Laboratoire d'Astrophysique de Marseille) UMR 7326, 13388, Marseille, France
[5] Astrophysics Group, Cavendish Laboratory, University of Cambridge, J J Thomson Avenue, Cambridge CB3 0HE, U.K.
[6] CGEE, SCS Qd 9, Lote C, Torre C, 4° andar, Ed. Parque Cidade Corporate, CEP 70308-200, Brasília, DF, Brazil
[7] CITA, University of Toronto, 60 St. George St., Toronto, ON M5S 3H8, Canada
[8] CNRS, IRAP, 9 Av. colonel Roche, BP 44346, F-31028 Toulouse cedex 4, France
[9] California Institute of Technology, Pasadena, California, U.S.A.
[10] Centro de Estudios de Física del Cosmos de Aragón (CEFCA), Plaza San Juan, 1, planta 2, E-44001, Teruel, Spain
[11] Computational Cosmology Center, Lawrence Berkeley National Laboratory, Berkeley, California, U.S.A.
[12] DSM/Irfu/SPP, CEA-Saclay, F-91191 Gif-sur-Yvette Cedex, France
[13] DTU Space, National Space Institute, Technical University of Denmark, Elektrovej 327, DK-2800 Kgs. Lyngby, Denmark
[14] Département de Physique Théorique, Université de Genève, 24, Quai E. Ansermet,1211 Genève 4, Switzerland
[15] Departamento de Astrofísica, Universidad de La Laguna (ULL), E-38206 La Laguna, Tenerife, Spain
[16] Departamento de Física, Universidad de Oviedo, Avda. Calvo Sotelo s/n, Oviedo, Spain
[17] Departamento de Matemáticas, Estadística y Computación, Universidad de Cantabria, Avda. de los Castros s/n, Santander, Spain
[18] Department of Astrophysics/IMAPP, Radboud University Nijmegen, P.O. Box 9010, 6500 GL Nijmegen, The Netherlands
[19] Department of Physics & Astronomy, University of British Columbia, 6224 Agricultural Road, Vancouver, British Columbia, Canada
[20] Department of Physics and Astronomy, Dana and David Dornsife College of Letter, Arts and Sciences, University of Southern California, Los Angeles, CA 90089, U.S.A.
[21] Department of Physics and Astronomy, University College London, London WC1E 6BT, U.K.
[22] Department of Physics, Florida State University, Keen Physics Building, 77 Chieftan Way, Tallahassee, Florida, U.S.A.
[23] Department of Physics, Gustaf Hällströmin katu 2a, University of Helsinki, Helsinki, Finland
[24] Department of Physics, Princeton University, Princeton, New Jersey, U.S.A.
[25] Department of Physics, University of California, Santa Barbara, California, U.S.A.
[26] Department of Physics, University of Illinois at Urbana-Champaign, 1110 West Green Street, Urbana, Illinois, U.S.A.
[27] Dipartimento di Fisica e Astronomia G. Galilei, Università degli Studi di Padova, via Marzolo 8, 35131 Padova, Italy
[28] Dipartimento di Fisica e Scienze della Terra, Università di Ferrara, Via Saragat 1, 44122 Ferrara, Italy
[29] Dipartimento di Fisica, Università La Sapienza, P. le A. Moro 2, Roma, Italy
[30] Dipartimento di Fisica, Università degli Studi di Milano, Via Celoria, 16, Milano, Italy
[31] Dipartimento di Fisica, Università degli Studi di Trieste, via A. Valerio 2, Trieste, Italy
[32] Dipartimento di Matematica, Università di Roma Tor Vergata, Via della Ricerca Scientifica, 1, Roma, Italy
[33] Discovery Center, Niels Bohr Institute, Blegdamsvej 17, Copenhagen, Denmark
[34] European Space Agency, ESAC, Planck Science Office, Camino bajo del Castillo, s/n, Urbanización Villafranca del Castillo, Villanueva de la Cañada, Madrid, Spain
[35] European Space Agency, ESTEC, Keplerlaan 1, 2201 AZ Noordwijk, The Netherlands
[36] Gran Sasso Science Institute, INFN, viale F. Crispi 7, 67100 L'Aquila, Italy
[37] HGSFP and University of Heidelberg, Theoretical Physics Department, Philosophenweg 16, 69120, Heidelberg, Germany
[38] Haverford College Astronomy Department, 370 Lancaster Avenue, Haverford, Pennsylvania, U.S.A.
[39] Helsinki Institute of Physics, Gustaf Hällströmin katu 2, University of Helsinki, Helsinki, Finland
[40] INAF - Osservatorio Astrofisico di Catania, Via S. Sofia 78, Catania, Italy
[41] INAF - Osservatorio Astronomico di Padova, Vicolo dell'Osservatorio 5, Padova, Italy
[42] INAF - Osservatorio Astronomico di Roma, via di Frascati 33, Monte Porzio Catone, Italy
[43] INAF - Osservatorio Astronomico di Trieste, Via G.B. Tiepolo 11, Trieste, Italy
[44] INAF/IASF Bologna, Via Gobetti 101, Bologna, Italy
[45] INAF/IASF Milano, Via E. Bassini 15, Milano, Italy
[46] INFN, Sezione di Bologna, Via Irnerio 46, I-40126, Bologna, Italy
[47] INFN, Sezione di Roma 1, Università di Roma Sapienza, Piazzale Aldo Moro 2, 00185, Roma, Italy
[48] INFN, Sezione di Roma 2, Università di Roma Tor Vergata, Via della Ricerca Scientifica, 1, Roma, Italy
[49] INFN/National Institute for Nuclear Physics, Via Valerio 2, I-34127 Trieste, Italy
[50] IUCAA, Post Bag 4, Ganeshkhind, Pune University Campus, Pune 411 007, India
[51] Imperial College London, Astrophysics group, Blackett Laboratory, Prince Consort Road, London, SW7 2AZ, U.K.
[52] Infrared Processing and Analysis Center, California Institute of Technology, Pasadena, CA 91125, U.S.A.
[53] Institut d'Astrophysique Spatiale, CNRS (UMR8617) Université Paris-Sud 11, Bâtiment 121, Orsay, France
[54] Institut d'Astrophysique de Paris, CNRS (UMR7095), 98 bis Boulevard Arago, F-75014, Paris, France

[55] Institute of Astronomy, University of Cambridge, Madingley Road, Cambridge CB3 0HA, U.K.
[56] Institute of Theoretical Astrophysics, University of Oslo, Blindern, Oslo, Norway
[57] Instituto de Astrofísica de Canarias, C/Vía Láctea s/n, La Laguna, Tenerife, Spain
[58] Instituto de Física de Cantabria (CSIC-Universidad de Cantabria), Avda. de los Castros s/n, Santander, Spain
[59] Istituto Nazionale di Fisica Nucleare, Sezione di Padova, via Marzolo 8, I-35131 Padova, Italy
[60] Jet Propulsion Laboratory, California Institute of Technology, 4800 Oak Grove Drive, Pasadena, California, U.S.A.
[61] Jodrell Bank Centre for Astrophysics, Alan Turing Building, School of Physics and Astronomy, The University of Manchester, Oxford Road, Manchester, M13 9PL, U.K.
[62] Kavli Institute for Cosmological Physics, University of Chicago, Chicago, IL 60637, USA
[63] Kavli Institute for Cosmology Cambridge, Madingley Road, Cambridge, CB3 0HA, U.K.
[64] Kazan Federal University, 18 Kremlyovskaya St., Kazan, 420008, Russia
[65] LAL, Université Paris-Sud, CNRS/IN2P3, Orsay, France
[66] LERMA, CNRS, Observatoire de Paris, 61 Avenue de l'Observatoire, Paris, France
[67] Laboratoire AIM, IRFU/Service d'Astrophysique - CEA/DSM - CNRS - Université Paris Diderot, Bât. 709, CEA-Saclay, F-91191 Gif-sur-Yvette Cedex, France
[68] Laboratoire de Physique Subatomique et Cosmologie, Université Grenoble-Alpes, CNRS/IN2P3, 53, rue des Martyrs, 38026 Grenoble Cedex, France
[69] Laboratoire de Physique Théorique, Université Paris-Sud 11 & CNRS, Bâtiment 210, 91405 Orsay, France
[70] Lawrence Berkeley National Laboratory, Berkeley, California, U.S.A.
[71] Max-Planck-Institut für Astrophysik, Karl-Schwarzschild-Str. 1, 85741 Garching, Germany
[72] National University of Ireland, Department of Experimental Physics, Maynooth, Co. Kildare, Ireland
[73] Nicolaus Copernicus Astronomical Center, Bartycka 18, 00-716 Warsaw, Poland
[74] Niels Bohr Institute, Blegdamsvej 17, Copenhagen, Denmark
[75] SISSA, Astrophysics Sector, via Bonomea 265, 34136, Trieste, Italy
[76] SMARTEST Research Centre, Università degli Studi e-Campus, Via Isimbardi 10, Novedrate (CO), 22060, Italy
[77] School of Physics and Astronomy, Cardiff University, Queens Buildings, The Parade, Cardiff, CF24 3AA, U.K.
[78] Space Sciences Laboratory, University of California, Berkeley, California, U.S.A.
[79] Special Astrophysical Observatory, Russian Academy of Sciences, Nizhnij Arkhyz, Zelenchukskiy region, Karachai-Cherkessian Republic, 369167, Russia
[80] Sub-Department of Astrophysics, University of Oxford, Keble Road, Oxford OX1 3RH, U.K.
[81] UPMC Univ Paris 06, UMR7095, 98 bis Boulevard Arago, F-75014, Paris, France
[82] Université de Toulouse, UPS-OMP, IRAP, F-31028 Toulouse cedex 4, France
[83] University of Granada, Departamento de Física Teórica y del Cosmos, Facultad de Ciencias, Granada, Spain
[84] University of Granada, Instituto Carlos I de Física Teórica y Computacional, Granada, Spain
[85] Warsaw University Observatory, Aleje Ujazdowskie 4, 00-478 Warszawa, Poland